

**Chandra X-ray analysis of the massive high-redshift galaxy
clusters ClJ1113.1–2615 and ClJ0152.7–1357**

B. J. Maughan

*School of Physics and Astronomy, University of Birmingham, Edgbaston, Birmingham,
B15 2TT, UK*

`bjm@star.sr.bham.ac.uk`

and

L. R. Jones

*School of Physics and Astronomy, University of Birmingham, Edgbaston, Birmingham,
B15 2TT, UK*

and

H. Ebeling

Institute for Astronomy, 2680 Woodlawn Drive, Honolulu, HI 96822, USA

and

E. Perlman¹

*Joint Centre for Astrophysics, Physics Department, University of Maryland, Baltimore
County, 1000 Hilltop Circle, Baltimore, MD 21250, USA*

and

P. Rosati

*European Southern Observatory (ESO), Headquarters, Karl-Schwarzschild-Strasse 2,
Garching D-85748, Germany*

and

C. Frye

¹Department of Physics & Astronomy, Johns Hopkins University, 3400 North Charles Street, Baltimore, MD 21218, USA

*Joint Centre for Astrophysics, Physics Department, University of Maryland, Baltimore
County, 1000 Hilltop Circle, Baltimore, MD 21250, USA*

and

C. R. Mullis

*European Southern Observatory (ESO), Headquarters, Karl-Schwarzschild-Strasse 2,
Garching D-85748, Germany*

ABSTRACT

We present an analysis of *Chandra* observations of two high-redshift clusters of galaxies, ClJ1113.1–2615 at $z = 0.725$ and ClJ0152.7–1357 at $z = 0.833$. We find ClJ1113.1–2615 to be morphologically relaxed with a temperature of $kT = 4.3_{-0.4}^{+0.5}$ keV and a mass (within the virial radius) of $4.3_{-0.7}^{+0.8} \times 10^{14} M_{\odot}$. ClJ0152.7–1357, by contrast, is resolved into a northern and southern subcluster, each massive and X-ray luminous, in the process of merging. The temperatures of the subclusters are found to be $5.5_{-0.8}^{+0.9}$ keV and $5.2_{-0.9}^{+1.1}$ keV respectively, and we estimate their respective masses to be $6.1_{-1.5}^{+1.7} \times 10^{14} M_{\odot}$ and $5.2_{-1.4}^{+1.8} \times 10^{14} M_{\odot}$ within the virial radii. A dynamical analysis of the system shows that the subclusters are likely to be gravitationally bound. If the subclusters merge they will form a system with a mass similar to that of the Coma cluster. Two-dimensional modelling of the X-ray surface brightness reveals excess emission between the subclusters; suggestive, but not conclusive evidence of a shock front.

We make a first attempt at measuring the cluster M-T relation at $z \approx 0.8$, and find no evolution in its normalisation, supporting the previous assumption of an unevolving M-T relation when constraining cosmological parameters from cluster evolution studies. A comparison of the cluster properties with those of nearby systems also finds little or no evolution in the L-T relation, the gas fraction-T relation, the β -T relation or the metallicity. These results suggest that, in at least some massive clusters, the hot gas was in place, and containing its metals, at $z \approx 0.8$, and thus that they were assembled at redshifts significantly higher than $z = 0.8$, as predicted in low Ω_M models.

We also highlight the need to correct for the degradation of the *Chandra* ACIS low energy quantum efficiency in high-redshift cluster studies when the low energy absorption is often assumed to be the Galactic value, rather than measured.

Subject headings: cosmology: observations – galaxies: clusters: general – galaxies: high-redshift galaxies: clusters: individual: (ClJ1113.1–2615, ClJ0152.7–1357) – intergalactic medium – X-rays: galaxies

1. Introduction

Detailed X-ray studies of distant galaxy clusters have only recently become possible thanks to powerful new instruments aboard the *Chandra* and *XMM-Newton* satellites. These clusters represent the largest bound systems in the universe, and the study of their properties, both individually and as a population, allows different cosmological and structure formation models to be tested and constrained.

Many cosmological models describe the formation of structure in the Universe in terms of a hierarchical model, in which initial density perturbations (the distribution of which is usually assumed to be Gaussian) in the early universe grow under gravity, eventually forming the massive structures seen today. In this scenario, less massive systems form first. Then, through a combination of merging and the ongoing collapse of the slightly less dense surrounding regions, larger systems of galaxies, groups, and clusters of galaxies are formed. The immediately observable, luminous components of these systems act as tracers of the underlying distribution of dark matter, which comprises the majority of the mass in the universe. While the basic elements of this scenario are widely accepted, many important details, specifically the epoch and mode of cluster assembly, remain largely unknown. Massive clusters are especially useful for quantitative studies because their abundance at high redshifts is very sensitive to the matter density of the Universe, their evolution is predicted to be strongest, and – being the most luminous systems – they are the ones that are observationally most accessible.

The X-ray properties of galaxy clusters have been exploited as cosmological probes for many years, using, for example, their temperatures (*e.g.* Henry & Arnaud 1991; Henry 2000), luminosities (*e.g.* Jones et al. 1998; Borgani et al. 2001), and more recently, gas mass fractions (Allen et al. 2002; Ettori et al. 2003). Since the launch of *Chandra* and *XMM-Newton*, these properties of clusters can be much more accurately measured out to higher redshifts, enabling us to constrain cosmological parameters to much higher precision. *Chandra* observations in particular have also found new and sometimes unexpected features in clusters, such as cold fronts (*e.g.* Markevitch et al. 2000), radio cavities (*e.g.* McNamara et al. 2001), and shock fronts (*e.g.* Markevitch et al. 2002). The detailed study of individual clusters is an important step to compiling samples of high-redshift clusters with well constrained properties.

Both clusters discussed here, ClJ1113.1–2615 and ClJ0152.7–1357, were discovered in the Wide Angle *ROSAT* Pointed Survey (WARPS: Scharf et al. (1997)); ClJ0152.7–1357 was also discovered independently in the RDCS (Rosati et al. 1998) and SHARC (Romer et al. 2000) surveys. However, due to their high redshifts and the limitations of previous instruments, relatively little is known about their properties. Optical spectroscopy was performed on galaxies in the region of the *ROSAT* X-ray sources to measure their redshift

and to confirm their cluster status (Ebeling et al. 2000; Perlman et al. 2002). The *ROSAT* observations of ClJ0152.7–1357 have been analysed in some detail (Ebeling et al. 2000), and the cluster has also been the subject of both *BeppoSAX* observations (Della Ceca et al. 2000) and Sunyaev-Zel’dovich effect imaging (Joy et al. 2001). The recent *Chandra* observations of these clusters, presented here, both complement and extend this previous work, and the results of the different observations are compared later. These observations, along with *Chandra* and *XMM-Newton* observations of other high-redshift clusters, will form the basis of a study of the evolution of the X-ray temperature function, thereby constraining the value of Ω_M .

Section 2 describes the general data preparation and analysis methods applied to the *Chandra* data for both objects. Sections 3 and 4 detail the results obtained for ClJ1113.1–2615 and ClJ0152.7–1357 respectively, before we summarise and discuss these results in section 5.

We perform our analysis assuming two different cosmological models: a Λ CDM model with $\Omega_M = 0.3$, $\Omega_\Lambda = 0.7$ and $H_0 = 70 \text{ km s}^{-1} \text{ Mpc}^{-1}$, and an Einstein-de Sitter model with $H_0 = 50 \text{ km s}^{-1} \text{ Mpc}^{-1}$ and $\Omega_M = 1$ ($\Omega_\Lambda = 0$). The Einstein-de Sitter model was chosen to allow comparisons with earlier work. Unless otherwise stated, results are quoted for the Λ CDM cosmology, and all errors are quoted at the 68% confidence level.

2. Data Preparation and Analysis

Our two targets were observed with the ACIS-I array of the *Chandra* X-ray Observatory, and the same standard data preparation steps were followed for both clusters as described below. ClJ0152.7–1357 was observed on 2000 August 8 (ObsID 913) and ClJ1113.1–2615 was observed on 2000 August 13 (ObsID 915).

Both data sets were reprocessed by the standard pipeline software, removing bad events, and excluding *ASCA* grades 1, 5, and 7 (corresponding to diagonal split, “L”-shaped split, and 3-pixel horizontal split events). The data were then corrected to the appropriate gain map, and for any known aspect offsets. A background lightcurve with time bins of 400 s was produced and analysed. The lightcurve of ClJ0152.7–1357 showed only brief periods of enhanced background, while there was a significant flaring event in the observation of ClJ1113.1–2615. All time intervals during which the background was $> 3\sigma$ from the mean level were removed, leaving a useful time of 34 ks for ClJ0152.7–1357 and 88 ks for ClJ1113.1–2615. Point sources were identified with the CIAO wavelet detection algorithm, *wavdetect*.

2.1. Spectral Analysis

Spectra were extracted from circular regions centred on the clusters’ X-ray centroids, within a radius chosen from a preliminary radial profile of the emission to yield good signal-to-noise ratios (snr). These radii were typically $\sim 50''$ and are hereafter referred to as the spectral radii (r_s) of the clusters. The Redistribution Matrix File (RMF), which relates the incident photon energy to the output channel energy of the instrument, and the Ancillary Response File (ARF), which describes the dependence of effective area upon energy, both vary spatially across the detector. Since our extended sources cover regions described by several different RMFs and ARFs, a mean of each of these files, weighted by the source counts, was produced and used in the spectral analysis.

Background spectra were extracted from annuli surrounding the clusters, on the same CCD, excluding any point sources and pixels near the chip edges. An alternative method of obtaining background spectra from blank-sky datasets (Markevitch 2001) was also examined. This method has the advantage that the background spectra are extracted from the same region of the CCD as the source, thus eliminating potential systematic errors caused by the spatial variations of both the energy response and the effective area across the chip. Changes in the quiescent background between the time of the blank-sky observation and that of the science observation being analysed can be, approximately, corrected for by normalising the blank-sky data appropriately. The method remains, however, vulnerable to temporal variations in the spectrum of the particle background, and also cannot easily account for the known strong directional variation of the Galactic soft X-ray emission. A comparison of both methods showed small ($\sim 1\sigma$) differences in the values of the best-fit parameters. Given the compactness of our targets on an angular scale, we felt that the former method of using a background spectrum created from the same observation as the target involved approximations that were better understood, and so this method was used in all of the analyses detailed below.

It has recently become apparent that there has been a continuous degradation in the ACIS low energy quantum efficiency (QE) since the launch of *Chandra*. This is believed to be due to a build up of hydrocarbons on the optical filter, or the CCDs, which has the effect of introducing extra absorption below around 1 keV. In the context of our data, if unmodelled, this absorption leads to an overestimate in cluster temperatures. To account for this, an XSPEC absorption model ACISABS has been developed², and the spectra presented here were reanalysed with this model. The effect of the QE correction is examined in Appendix A.

²<http://www.astro.psu.edu/users/chartas/xcontdir/xcont.html>

The resulting spectra were fit with an absorbed MEKAL plasma emission model (Kaas-
tra & Mewe 1993; Liedahl et al. 1995) in both Sherpa and XSPEC (Arnaud 1996), with
completely consistent results. The normalisation of the MEKAL component was used to
calculate the central density of the intra-cluster gas, ρ_0 , as follows. The MEKAL normalisa-
tion in XSPEC is defined as

$$N_{mek} = \frac{10^{-14}}{4\pi D_a^2 (1+z)^2} \int n_e n_H dV \text{cm}^{-5}, \quad (1)$$

where D_a is the angular diameter distance in cm, and n_e and n_H are the central number
densities of electrons and hydrogen respectively. Under the assumption that the cluster
gas has a spherically symmetric density profile described by a β -profile (Cavaliere & Fusco-
Femiano 1976) (the parameters r_c and β of which are derived from the data as described in
the following section), we have

$$\rho(r) = \rho_0 \left(1 + \left(\frac{r}{r_c} \right)^2 \right)^{-3\beta/2}. \quad (2)$$

Considering that the spectrum is taken from a circular region of radius r_s , viewing the sphere
in projection, the integral of Eqn. 1 can be expressed as

$$\int 1.17 \rho^2 dV = 1.17 \left(\int_0^\infty \rho(r)^2 4\pi r^2 dr - \int_{r_s}^\infty \rho(r)^2 4\pi r^2 \left(1 - \left(\frac{r_s}{r} \right)^2 \right)^{0.5} dr \right). \quad (3)$$

Here we assume $n_e = 1.17n_H$. The central gas density ρ_0 can then be derived from the
MEKAL normalisation via Eqn. 1.

2.2. Spatial Analysis

The spatial analysis of the cluster X-ray emission was performed in the 0.5–5 keV energy
range within which the spectra, extracted as detailed in the preceding section, showed to
feature the highest snr. The spectra were also used to produce spectrally weighted exposure
maps³ for the imaging analysis.

³For *Chandra* data, the standard analysis software produces an exposure map that is an image of the
effective exposure time in units of s cm² in the detector plane, taking into account the vignetting of the
telescope, CCD gaps, the effective area of the telescope, and the dithering of the satellite. By producing a
spectrally weighted exposure map, in effect combining exposure maps in several energy ranges weighted by
the number of counts in each range, one also accounts for the energy dependence of the vignetting and of
the effective area.

Two kinds of models of the cluster emission were employed – a one-dimensional (1D) model of the radial surface-brightness profile assuming spherical symmetry, and a two-dimensional (2D) model of the emission which is fit to an image (see Birkinshaw et al. (*e.g.* 1991) for a discussion of 2D fitting). When producing a radial profile it is desirable to have $\gtrsim 20$ counts in each radial bin, so that Gaussian errors may be assumed⁴. When dividing a raw-counts image by an exposure map, the latter was normalised to its value at the cluster centroid, so that the exposure-corrected image maintains, as much as possible, the photon statistics of the recorded counts image. Since our exposure maps vary by typically no more than $\approx 5\%$ across the region of interest, this approach should not noticeably affect the accuracy of our results or their errors.

A second concern in any imaging analysis is the impact of the point spread function (PSF) of the telescope. In our 1D analysis we do not account for the PSF at all, because the *Chandra* PSF FWHM is smaller than the typical bin size in the radial profiles, so should have little effect. The 2D method deals more elegantly with both the exposure map and the PSF: the 2D model is convolved with a PSF model generated for the energy and off-axis position of the cluster, and then multiplied by the exposure map, before being compared with the original, unflattened image. This has the advantage of preserving the Poisson statistics of the observed image. The disadvantage of the 2D approach is that, since each image pixel contains very few (or zero) counts, we must use the C statistic (Cash 1979) to find the best fit. Unlike the χ^2 statistic, the value of the C statistic gives no measure of the absolute goodness of fit. The χ^2 statistic may be used though when fitting a radial profile, provided the radial bins contain sufficient counts. Thus the approach followed in our imaging analysis was to derive the best fit parameters and their errors with the 2D method, and use 1D profiles to check consistency and judge the goodness-of-fit.

In general, we model the surface-brightness distribution of each cluster, or subcluster, with a β -model given by

$$S(r) = S_0 \left(1 + \left(\frac{r}{r_c} \right)^2 \right)^{-3\beta+1/2}, \quad (4)$$

where $S(r)$ is the surface brightness at radius r , S_0 is the central surface brightness, r_c is the core radius, and β describes the slope of the profile at large radii. In the case of the 2D models, the eccentricity (e) and the rotation angle (θ) of the semi-major axis of the model relate the Cartesian (x,y) coordinates of a point in the image to the radial coordinate.

⁴For significances below 3σ , $n \geq 20$ ensures that the Gaussian approximation is accurate to better than 30 (10) % for the lower and upper limits, respectively, when compared to the exact Poisson errors (Ebeling 2002).

The integrated properties of the cluster gas (*i.e.* flux, luminosity and mass) were then estimated at the virial radius by extrapolating their values, measured within the spectral radius, using the measured model profile. The virial radius of a cluster may be estimated using self-similar scaling arguments, normalised to numerical simulations. Here, we adopted the formalism of Arnaud et al. (2002a), which may be applied to a flat ($\Omega_0 + \Lambda = 1$) or open ($\Omega_0 < 1, \Lambda = 0$) Universe:

$$r_v = 3.80 \beta_T^{1/2} \Delta_z^{-1/2} (1+z)^{-3/2} \times \left(\frac{kT}{10 \text{ keV}} \right)^{1/2} h_{50}^{-1} \text{ Mpc}. \quad (5)$$

Where $\Delta_z = (\Delta_c \Omega_0)/(18\pi^2 \Omega_z)$, $\beta_T = 1.05$ is a normalisation, taken from Evrard et al. (1996), and the density contrast Δ_c is given by

$$\Delta_c = 18\pi^2 + 60(\Omega_z - 1) - 32(\Omega_z - 1)^2 \quad (6)$$

for an open Universe, and

$$\Delta_c = 18\pi^2 + 82(\Omega_z - 1) - 39(\Omega_z - 1)^2 \quad (7)$$

for a flat Universe. The matter density at redshift z , Ω_z , is given by

$$\Omega_z = \frac{\Omega_0 (1+z)^3}{\Omega_0 (1+z)^3 + (1 - \Omega_0 - \Lambda) (1+z)^2 + \Lambda}. \quad (8)$$

The total gravitating mass of the cluster can then be estimated if we assume that the cluster is spherically symmetric, in hydrostatic equilibrium, and is well described by an isothermal β -profile. Adopting further a value of $0.59m_p$ for the mean molecular weight of the gas, where m_p is the proton mass, we can express the total mass of the cluster within a radius r as (Evrard et al. 1996),

$$M(r) = 1.13 \times 10^{14} \beta \frac{T}{\text{keV}} \frac{r}{\text{Mpc}} \frac{(r/r_c)^2}{1 + (r/r_c)^2} M_\odot. \quad (9)$$

2.3. Treatment of Errors

The errors of the measured fluxes (within the extraction regions) were calculated from the fractional errors on the normalisation of the spectrum; errors of all derived quantities were computed self-consistently with a ‘quasi Monte-Carlo method’ as follows. For each measured parameter T, β , and flux, an asymmetric Gaussian was computed, centred on the best-fit

value and with the positive and negative σ widths given by the positive and negative 1σ errors found from the best fits. 100,000 values were selected at random from these distributions to compute the distributions of each dependent quantity, such as L_X or M . The errors quoted for each quantity are the range within which $\pm 34\%$ of the values occurred. The core radius r_c was fixed during this process. The errors on β from the surface brightness fitting were computed with r_c free to vary, to account for the correlation between these variables. The contributions of the errors on r_c were found to be insignificant compared to those on β , and so were ignored. This method highlights the uncertainties involved in extrapolating the emission beyond the spectral radius: the extrapolation is strongly dependent on the slope of the surface-brightness profile. Lower values of β correspond to a shallower profile, with a smaller fraction of the emission being directly measured, leading to larger uncertainties on the extrapolated values, such as the scaled fluxes. The spread of values of β , therefore, contributes significantly to the errors on the scaled parameters.

3. Cluster ClJ1113.1–2615

This cluster was identified as a low-surface-brightness, extended X-ray source in the WARPS survey (Perlman et al. 2002). It has a high redshift of $z = 0.725$ giving a scale of 7.2 kpc per arcsecond (Λ CDM cosmology). In Fig. 1, contours of the X-ray emission detected by *Chandra* are overlaid on an optical I-band image, obtained at the Keck II 10 m telescope. The inner X-ray contours appear smooth and fairly regular, indicating that, at least in the central regions, the intra-cluster gas is in a relaxed state. This supports the assumption of hydrostatic equilibrium which underpins the derivation of several of the cluster’s properties, such as the mass and virial radius. The region shown in Fig. 1 contains one faint X-ray point source approximately $25''$ north-east of the cluster.

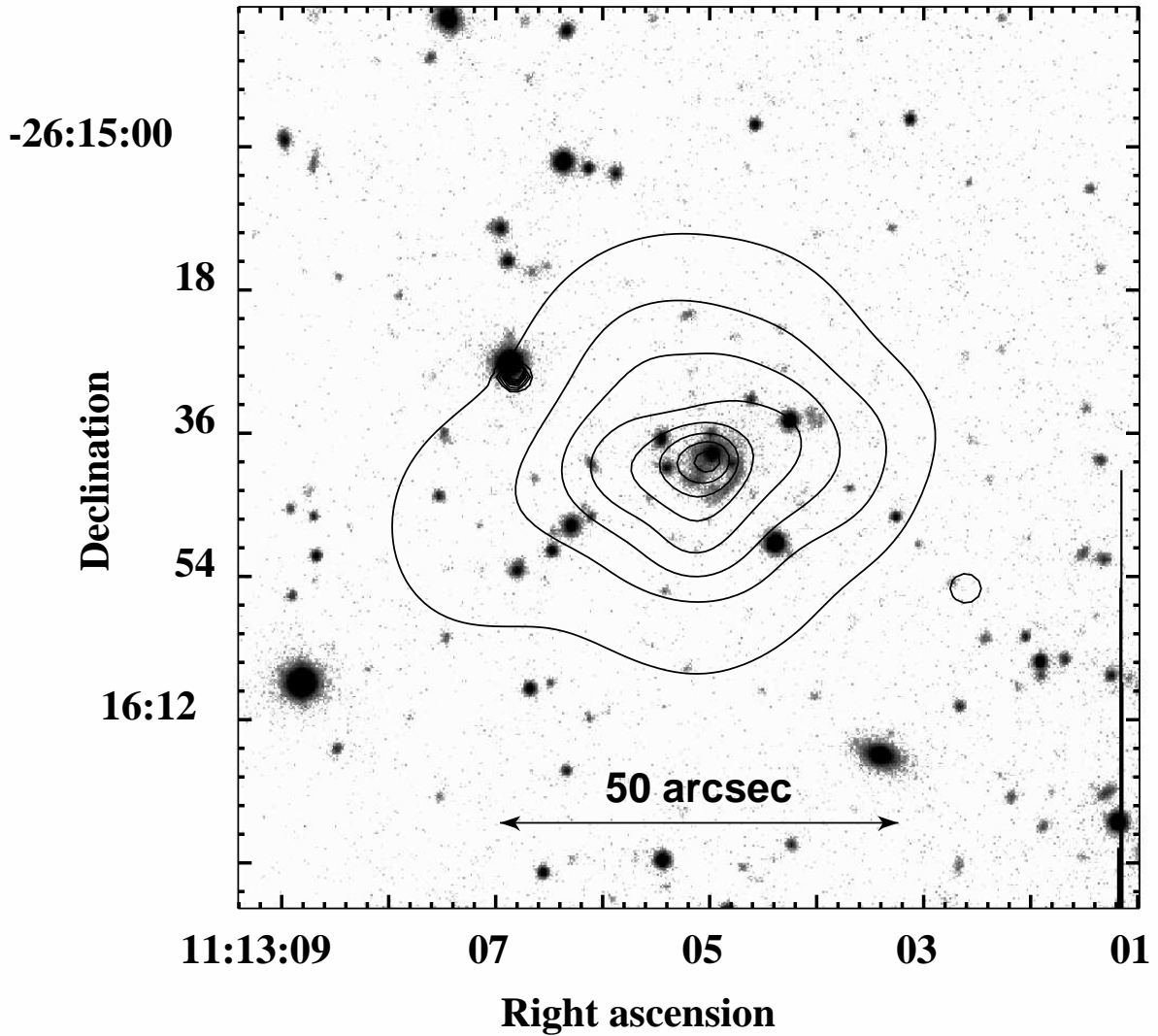


Fig. 1.— Adaptively smoothed *Chandra* X-ray contours overlaid on a Keck II (LRIS) I-band image of CIJ1113.1–2615. The contours were taken from an exposure corrected image, which was adaptively smoothed so that all features are significant at the 99% level. The contours start at 0.2 counts pixel⁻¹, and are logarithmically spaced by a factor of 1.2.

Fig. 2 indicates the regions used for the extraction of products. The rectangular regions are the source and background regions used in the imaging analysis, while the circle and annulus are the source and background regions, respectively, used in the spectral analysis. Note that the barred, dashed rectangular region indicates data along the CCD edge that were excluded from the spectral background. All point sources were excluded from the following spectral and imaging analysis.

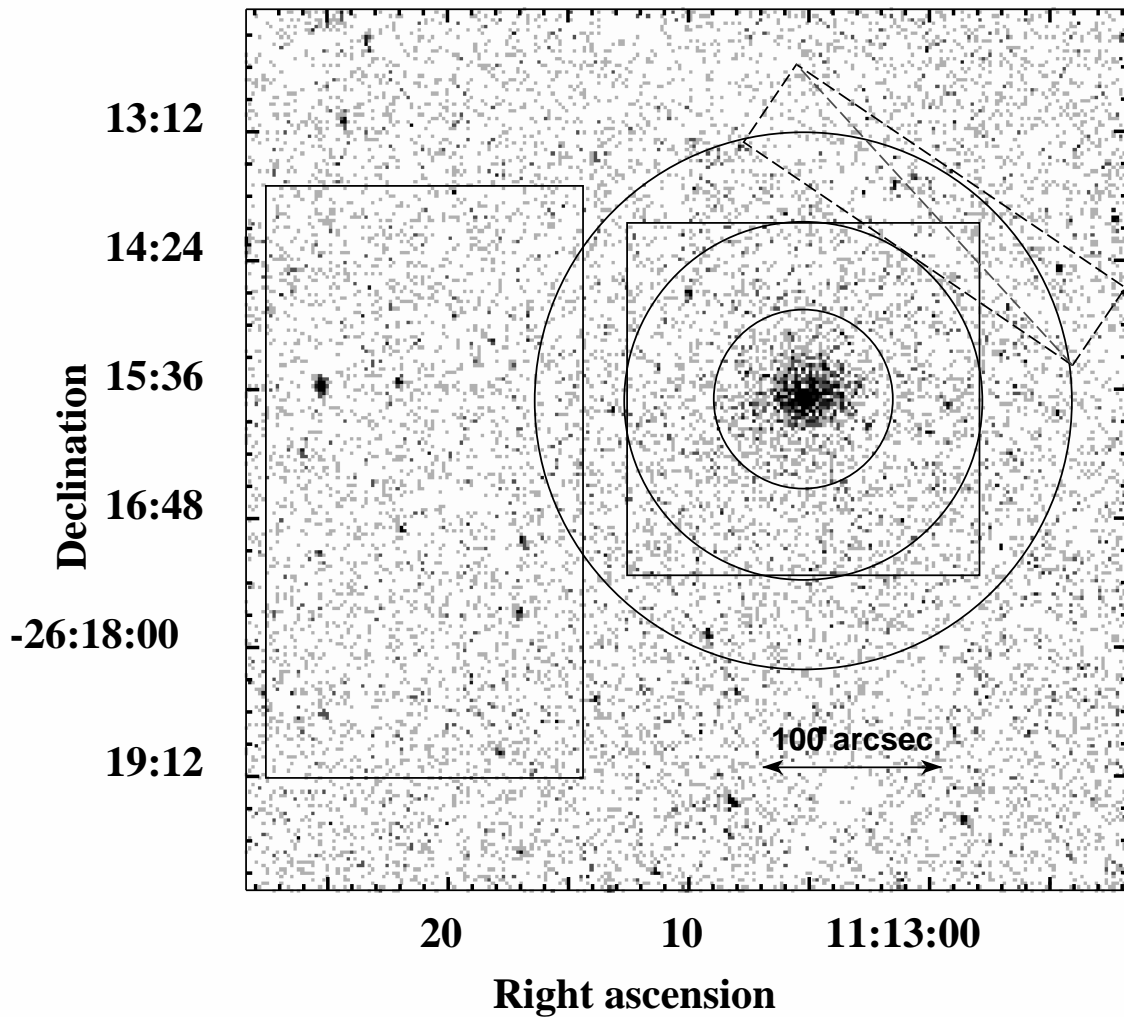


Fig. 2.— X-ray image of ClJ1113.1–2615 with pixels of $1.968''$. The regions used for imaging (rectangular) and spectral (circle and annulus) analysis are shown. The dashed rectangular region was ignored because it was close to a CCD edge.

3.1. Spectral results

An initial radial profile suggested a spectral radius of $50''$, and so a circular region of this size, centred on the X-ray centroid ($\alpha = 11^h 13^m 5^s 23$, $\delta = -26^\circ 15' 41'' 4$) and excluding a region of radius $2''$ around the point source to the north-east, was used to produce a spectrum containing around 1000 net counts. The spectrum was grouped to obtain a minimum of 20 counts per bin, and fit with an absorbed MEKAL model (including the ACISABS absorption model discussed in Appendix A), with the absorbing hydrogen column density frozen at the Galactic value of $5.47 \times 10^{20} \text{ cm}^{-2}$ (Dickey & Lockman 1990). The redshift was frozen at 0.725, and all fits were performed in the energy range of 0.5 – 8 keV. The spectrum and the best-fit model are shown in Fig. 3.

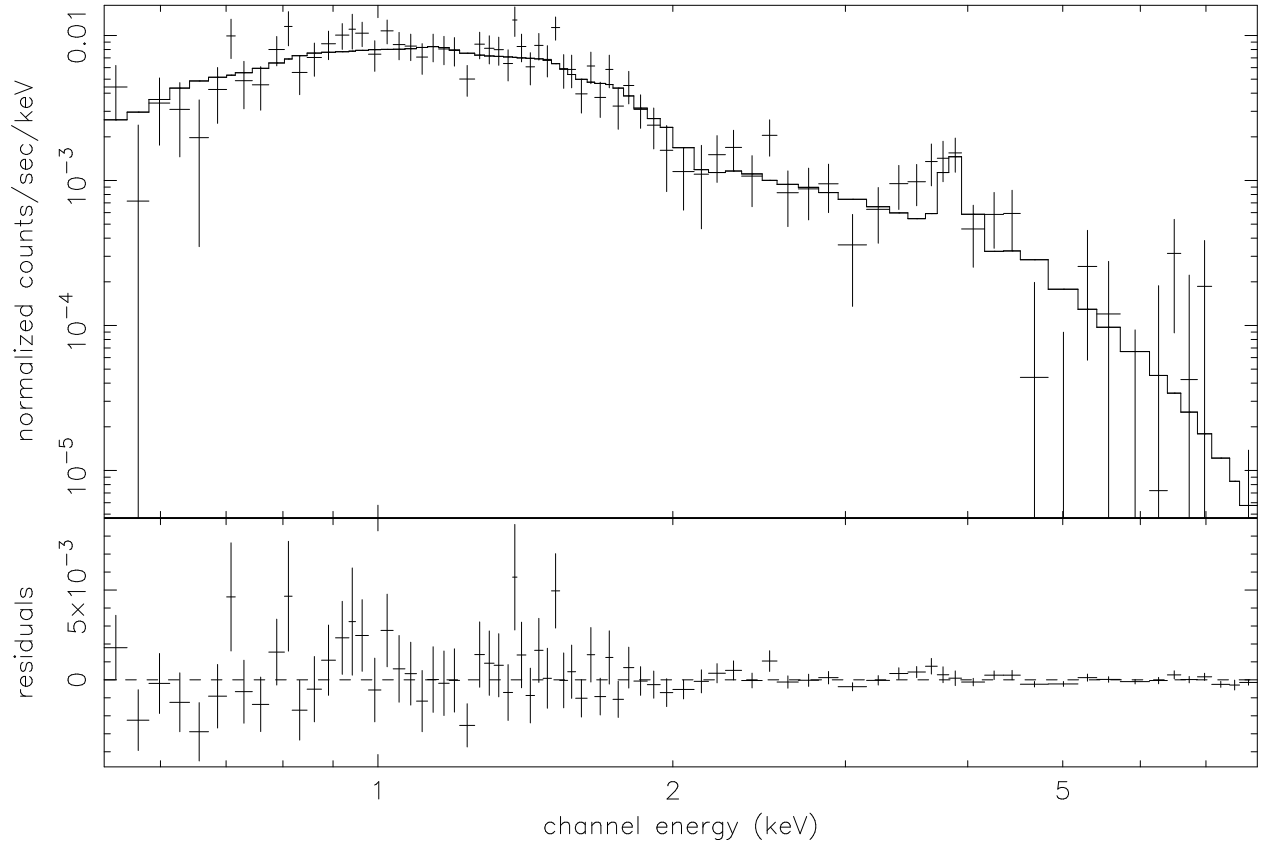


Fig. 3.— Spectrum and best-fit model of CIJ1113.1–2615.

The best fit to the spectrum was obtained for a temperature of $4.3_{-0.4}^{+0.5}$ keV and an abundance of $0.62_{-0.22}^{+0.25}$ solar, with a reduced χ^2 value of 1.00 (62 degrees of freedom). We repeated the fit with the abundance frozen at the canonical value of 0.3, and found a temperature of $4.4_{-0.5}^{+0.7}$ keV and a reduced χ^2 value of 1.02 (63 degrees of freedom). A redshifted iron line is prominent at 3.8 keV. Thawing the redshift parameter of the spectral model led to a best fit for a value of $z = 0.745_{-0.015}^{+0.084}$, which is higher than the optically derived value of $z = 0.725$ but not significantly so. Similar redshift differences have been observed in the *Chandra* spectra of other clusters (*e.g.* Schindler et al. 2001) and are likely to be due to calibration errors. If so, such errors in the position of the spectral lines will also affect the spectral fits of the metallicities. However, as the differences in the fit parameters caused by freezing, or fitting the metal abundance are well within their 1σ errors, we use those values derived with the fitted metallicity in our further analysis.

A hardness ratio map of the cluster was produced by creating images in the energy bands 0.5 – 1.5 keV (soft band) and 1.5 – 8 keV (hard band), subtracting a constant background level in each energy band, and dividing the hard image by the soft image. The images were both exposure corrected with the same, broad band exposure map. Strictly, they should be corrected by exposure maps generated for the same range of energies as the images, however this is a very small effect compared to the large errors due to counting statistics. The low number of photons available forced a large pixel size to be used in order to reach ≥ 20 counts per pixel, so the resolution of the image was low (110 kpc/pixel). Spectra were simulated, using an absorbed MEKAL model at the cluster redshift, for a series of temperatures, and the number of photons in the hard and soft bands defined above were divided to give a hardness ratio. In this way, a look-up table was constructed, that allowed the conversion of the measured hardness ratios into temperatures. The limits of the data allow us only to state that the cluster shows no significant departures from a temperature of 5 ± 3 keV on scales of ~ 100 kpc. In particular, there is no evidence for a central cooling flow, although the constraints are weak.

3.2. Spatial results

The cluster X-ray emission was then examined spatially, as described in section 2.2. The source model included a constant background flux of 3.95×10^{-10} counts $\text{cm}^{-2} \text{s}^{-1}$ which was estimated from an independent 2D fit to a background region of the same CCD. Four point sources in the fitting regions were masked out. After convolution with an appropriate PSF model and multiplication with an appropriate exposure map, the model was fit to the data in Sherpa using a maximum-likelihood algorithm and the C statistic. The best-fit model

parameters were $r_c = 14.6_{-2.2}^{+1.2''}$ (105_{-16}^{+9} kpc), $\beta = 0.67_{-0.05}^{+0.03}$, and $e = 0.2$. The background level was also allowed to fit, which gave no significant change to the best fitting parameters. Errors were computed with all parameter values free to vary, but were not computed for the eccentricity because of the computational load involved.

The image was then divided by a normalised exposure map to produce a exposure corrected image (with units of counts), and a radial profile was produced excluding the same point sources, estimating the background from the same region as the 2D fitting, and centred on the best-fit position of the 2D model. The radial bins were adaptively sized so that their minimal width was 2 pixels ($\approx 1''$) and the minimal snr value per bin was 3. Emission was detected at this level out to a radius of $92.0''$, which is similar to the size of the region within which the 2D fitting was performed. The best-fit parameters of a β -profile fit to these data are $r_c = 10.5_{-1.2}^{+1.3''}$ (76_{-9}^{+9} kpc) and $\beta = 0.58_{-0.03}^{+0.03}$, with a reduced χ^2 value of 1.6 (46 degrees of freedom). These fit results do not agree well with those of the 2D fit, however, it is easily shown that the disagreement is due to the eccentricity of the cluster emission. An image of the best-fitting 2D model, convolved with the PSF and multiplied with the exposure map, was used to produce a radial profile in exactly the same manner as above. We obtained best-fit values of $r_c = 11.2_{-1.1}^{+1.2''}$ (81_{-9}^{+9} kpc) and $\beta = 0.60_{-0.03}^{+0.03}$, in good agreement with those found for the radial profile of the real data. We thus consider the most reliable measurements to be those from the 2D fit. The radial profile, best-fitting β -model, and profile of the best-fitting 2D model are shown in Fig. 4.

The reduced χ^2 statistic of 1.6 indicates that the 1D fit is not a very good one, however, given that we are fitting a circular model to an elliptical cluster, and that the profile of the 2D model appears to agree well with the data, we believe that the 2D model is a good description of the data.

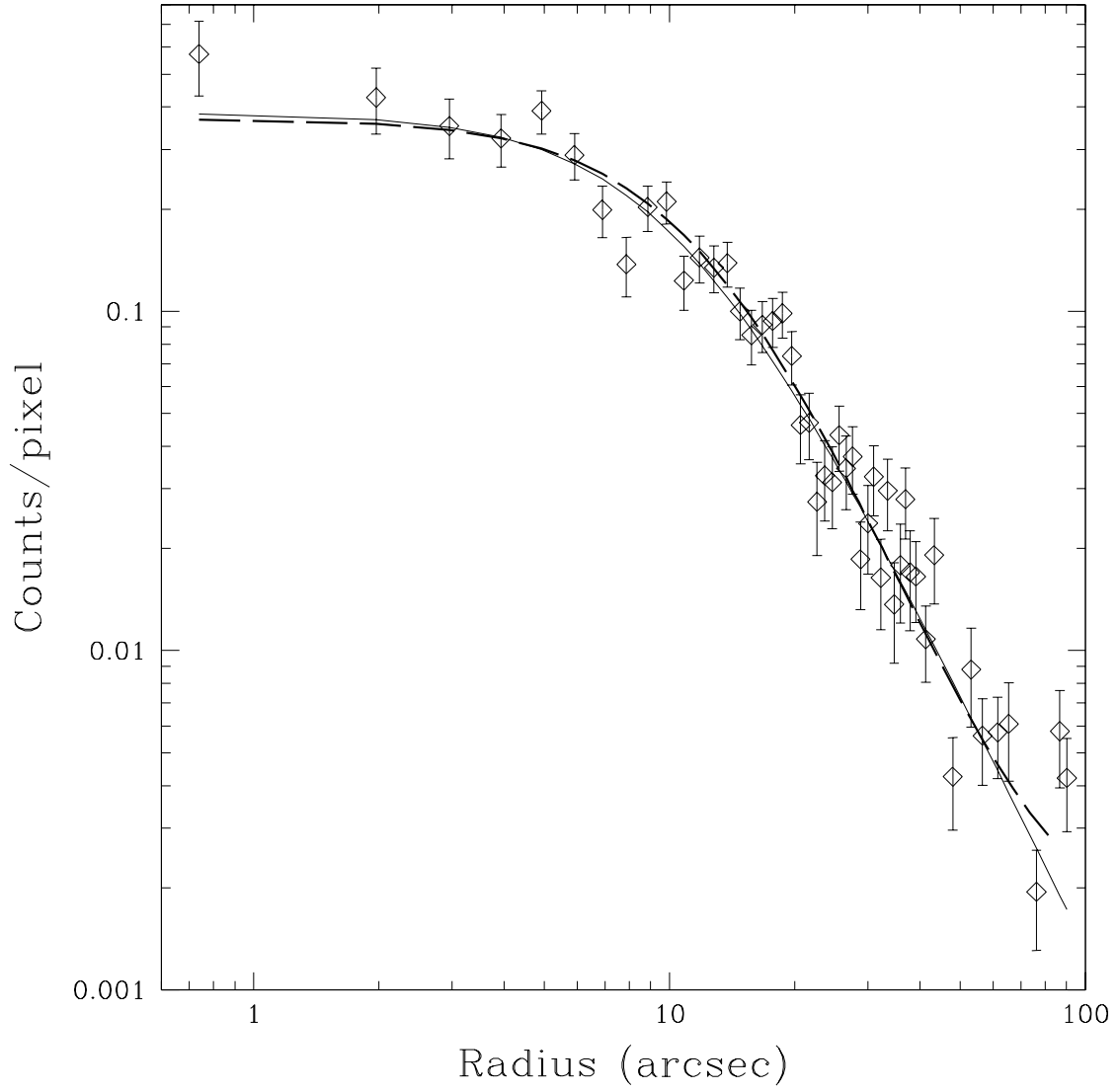


Fig. 4.— Surface-brightness profile of ClJ1113.1–2615. The solid line shows the best-fit 1D β -model, and the dashed line shows a profile of the best-fitting 2D model.

To better examine any discrepancies between the data and our β -model, we subtracted the best-fitting 2D model from the data, and smoothed the resulting image with a Gaussian kernel of fixed size $\sigma = 3''$, thus producing a residual map. The residuals are evenly distributed with no significant features, again indicating that the 2D fit provides a good description of the data.

Using Eqn. 5 we estimate the virial radius of the cluster to be 1.3 ± 0.1 Mpc. Our 1D analysis of the X-ray surface brightness detects cluster emission out to approximately 51% of this value, whereas the spectral radius, within which the immediately detected flux is measured, corresponds to only $\approx 27\%$ of the virial radius. In order to estimate the total flux, and hence the total luminosity of the cluster, the observed flux was extrapolated out to the virial radius using the best-fit β -model. To allow comparisons with other work, this extrapolation was carried out in both of our chosen cosmologies (the value of r_v is cosmology dependent, as is the conversion between the angular and physical size of the spectral radius). We found the scaling factor to be ≈ 1.3 for either cosmology. The bolometric, unabsorbed, total cluster flux is thus $F(r_v) = 1.38_{-0.12}^{+0.13} \times 10^{-13}$ erg s $^{-1}$ cm $^{-2}$, corresponding to a bolometric luminosity of $L(r_v) = 3.3_{-0.3}^{+0.3} \times 10^{44}$ erg s $^{-1}$ (Λ CDM cosmology).

In order to allow a comparison of the result from the flux measurement with *Chandra* with those of previous observations, we also extrapolated to the virial radius the unabsorbed flux in the 0.5 – 2 keV band using our alternative Einstein-de Sitter cosmology. We find $F(r_v) = 5.7 \pm 0.5 \times 10^{-14}$ erg s $^{-1}$ cm $^{-2}$, which is marginally lower than the value of $7.4 \pm 1.1 \times 10^{-14}$ erg s $^{-1}$ cm $^{-2}$ measured with *ROSAT* (Perlman et al. 2002). This lower flux can be explained by the exclusion of point sources in this analysis that were not resolved by *ROSAT*. *Chandra* resolves 5 point sources in the region where the *ROSAT* flux was measured. The fluxes of these sources were estimated, assuming the best fitting spectral model to the brightest point source within 2 Mpc of the cluster. This was a absorbed power law, with a photon index $\gamma = 2.09 \pm 0.05$. The combined 0.5 – 2 keV flux in these five point sources was 1.3×10^{-14} erg s $^{-1}$ cm $^{-2}$, which brings the *Chandra* flux up to $F(r_v) = 7.0 \pm 0.5 \times 10^{-14}$ erg s $^{-1}$ cm $^{-2}$, in good agreement with the *ROSAT* flux.

For further comparison with other work (section 5), the bolometric luminosity was also computed for an Einstein-de Sitter cosmology, giving a value of $3.9_{-0.3}^{+0.4} \times 10^{44}$ erg s $^{-1}$.

The central hydrogen number density in ClJ1113.1–2615 was found to be $n_H = 7.3 \pm 0.6 \times 10^{-3}$ cm $^{-3}$, giving a gas mass within the spectral radius, and extrapolated out to the virial radius, of $M_g(r_s) = 5.7_{-0.2}^{+0.2} \times 10^{12} M_\odot$ and $M_g(r_v) = 3.0_{-0.4}^{+0.4} \times 10^{13} M_\odot$, respectively. The total gravitating mass of the cluster is estimated at $M(r_s) = 1.1_{-1.2}^{+1.4} \times 10^{13} M_\odot$ within the spectral radius of ClJ1113.1–2615; extrapolating to the virial radius we find $M(r_v) = 4.3 \pm 0.1 \times 10^{14} M_\odot$. This gives a gas mass fraction (M_g/M) within the spectral radius

of 0.05 ± 0.01 , and of 0.07 ± 0.01 within the virial radius. A comparison of these cluster properties with those measured for a sample of local groups and clusters is performed in section 5.

4. Cluster ClJ0152.7–1357

Upon its discovery in archival *ROSAT* PSPC data, ClJ0152.7–1357 was the most X-ray luminous distant ($z > 0.8$) cluster known (Ebeling et al. 2000). Its X-ray morphology as seen with *ROSAT* strongly suggested complex substructure, possibly the result of a merger in progress. At the cluster redshift of $z = 0.833$ 1 arcsecond corresponds to 7.6 kpc (Λ CDM). Fig. 5 shows *Chandra* X-ray contours overlaid on a Keck II (LRIS) I-band image of the cluster. The contours clearly show two peaks of X-ray emission, coincident with two concentrations of galaxies. It appears that the contours are more tightly grouped along the south-west edge of the northern subcluster, and more extended to the north-east. This is suggestive of the northern subcluster moving toward the southern cluster component.

It is interesting to note that the inner contours of the southern subcluster are displaced to the south of the subcluster galaxies, with the local X-ray centroid $\sim 5''$ south of the galaxies. The astrometry of both the optical and X-ray data (using X-ray point sources in the field of view) were checked against the Automatic Plate Measuring (APM) source catalogue, and found to be accurate to within $\sim 0.5''$; hence the displacement appears to be real. Similar displacements have been observed in other merging galaxy clusters (*e.g.* Markevitch et al. 2002), and can be explained by the collisionless galaxies (and presumably dark matter) moving ahead of the ICM which is slowed by ram pressure.

The X-ray centroids of the two subclusters (North: $\alpha = 1^h52^m44^s18$, $\delta = -13^\circ57'15''.84$; South: $\alpha = 1^h52^m39^s89$, $\delta = -13^\circ58'27''.48$) are $95''$ apart, equivalent to 722 kpc in our Λ CDM cosmology. The question of whether the two subclusters are gravitationally bound is addressed later in this section.

There is also a region of extended low surface brightness emission to the east of the cluster ($\alpha = 1^h52^m52^s42$, $\delta = -13^\circ58'5''.52$) associated with an overdensity of galaxies. Three galaxy redshifts confirm the existence of a group of galaxies at $z = 0.844 \pm 0.002$ (Demarco et al. 2002). The limited statistics of both the optical and X-ray data prohibit detailed investigation of this system, but it would appear to be an infalling galaxy group. Note that this feature is not visible within the field of Fig. 5.

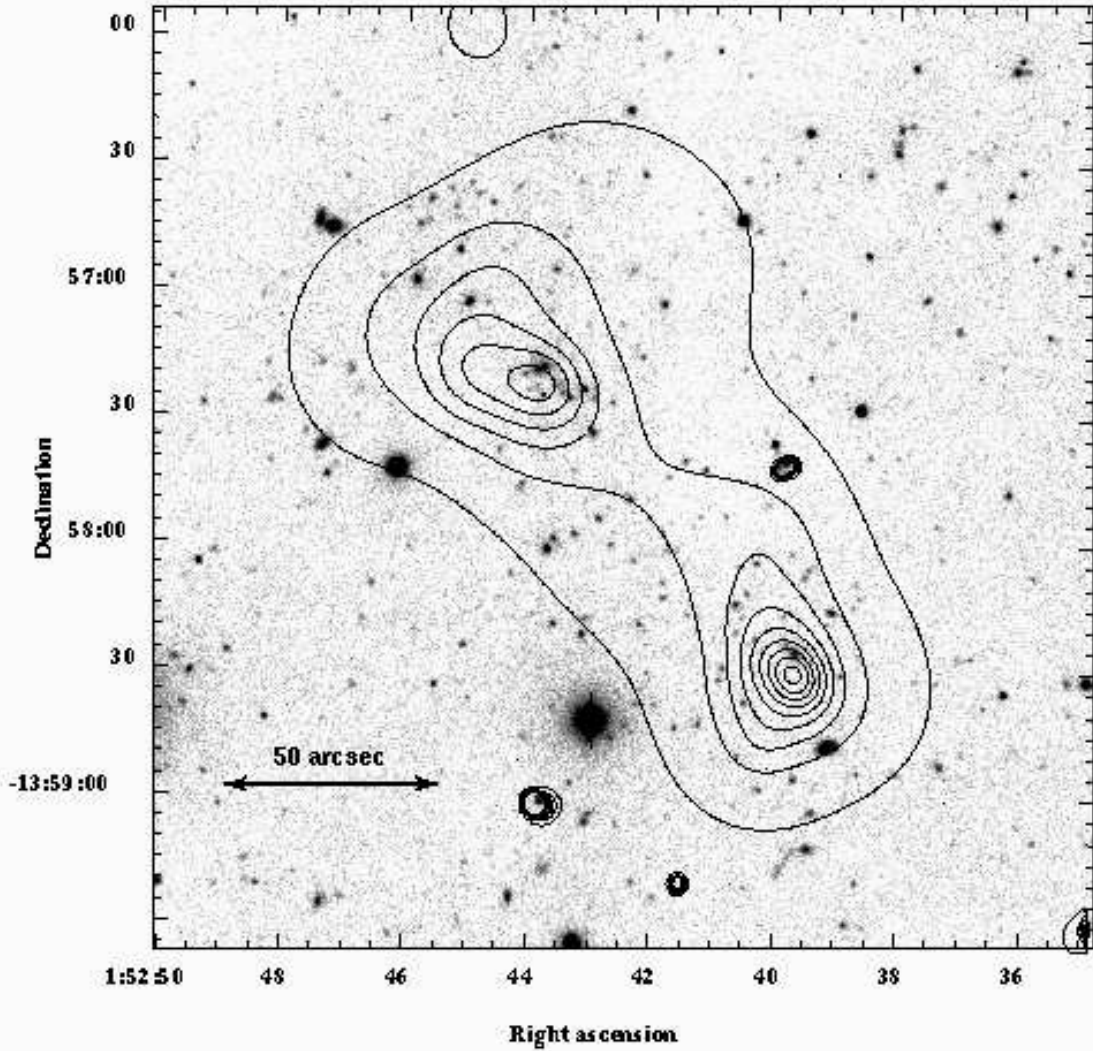


Fig. 5.— Adaptively smoothed *Chandra* X-ray contours overlaid on a Keck II I-band image of CIJ0152.7–1357. The contours were produced from an exposure corrected image in the energy band 0.5–5 keV, which was adaptively smoothed so that all features were significant at the 99% level. The contours start at 0.03 counts pixel⁻¹, and are logarithmically spaced, by a factor of 1.5.

The regions used for the extraction of different products are shown in Fig. 6, overlaid on a binned X-ray image. The circular regions were used to extract the source spectra, with the elliptical annulus as a background (excluding the dashed, barred rectangular regions). The non-barred rectangular regions were used for the imaging analysis. Point sources were excluded from all spectral and imaging analysis.

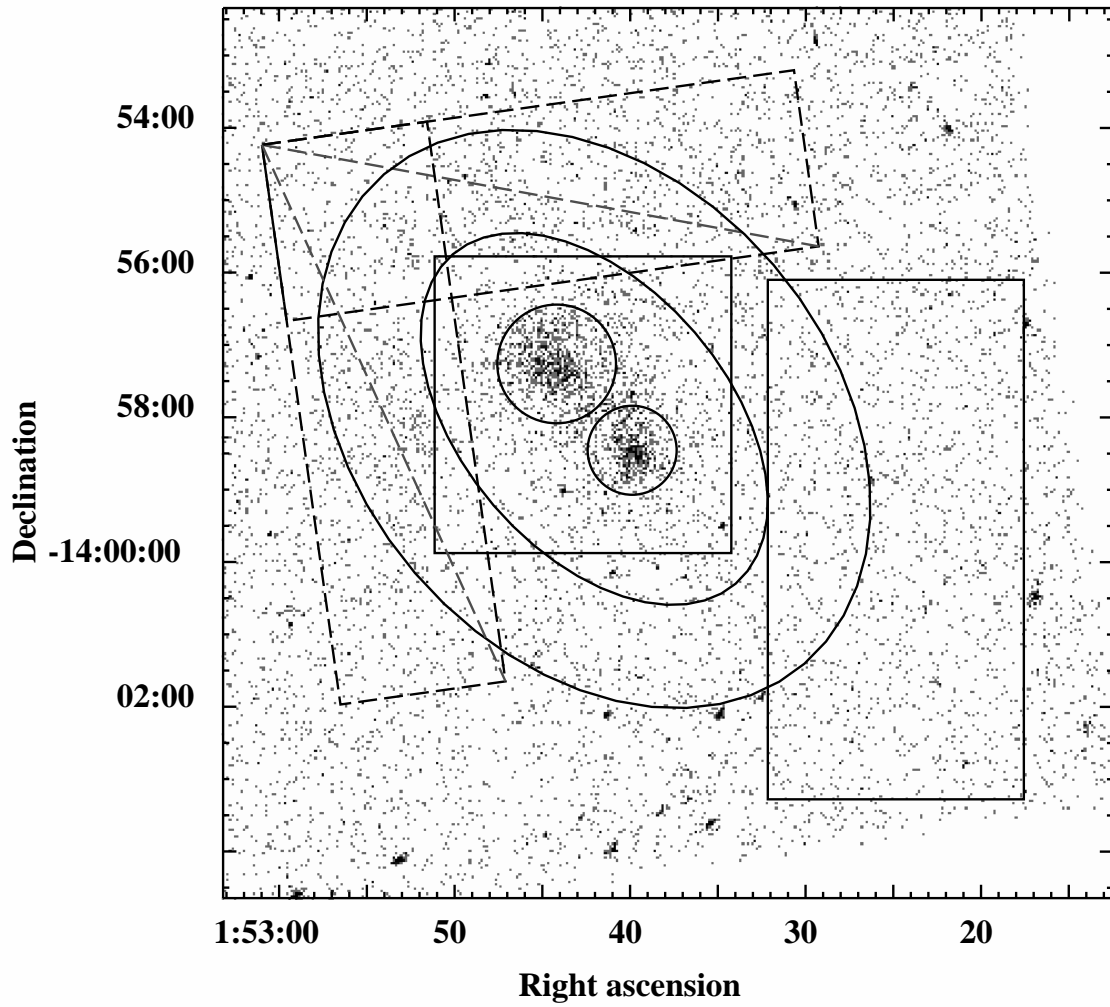


Fig. 6.— Chandra X-ray image of ClJ0152.7–1357 with pixels of $2''$. The regions used for imaging and spectral analysis are shown (see text).

4.1. Spectral results

Spectra were extracted within circular regions of radius $49''$ and $37''$ of the centroids of the northern and southern subcluster respectively, and were fit with an absorbed MEKAL model (again including the ACISABS absorption model discussed in Appendix A). The northern cluster region contained around 750 net counts, and the southern cluster around 450. The absorbing hydrogen column density was frozen at the Galactic value (Dickey & Lockman 1990) for the position of each of the subcluster centroids (north: $1.55 \times 10^{20} \text{cm}^{-2}$, south: $1.54 \times 10^{20} \text{cm}^{-2}$). The MEKAL redshift was frozen at 0.833 for both cluster components, and the spectra were fit in the 0.5 – 8 keV energy range, after having being grouped into bins containing ≥ 20 counts each. The spectra and best-fit models are shown in Figs. 7 and 8.

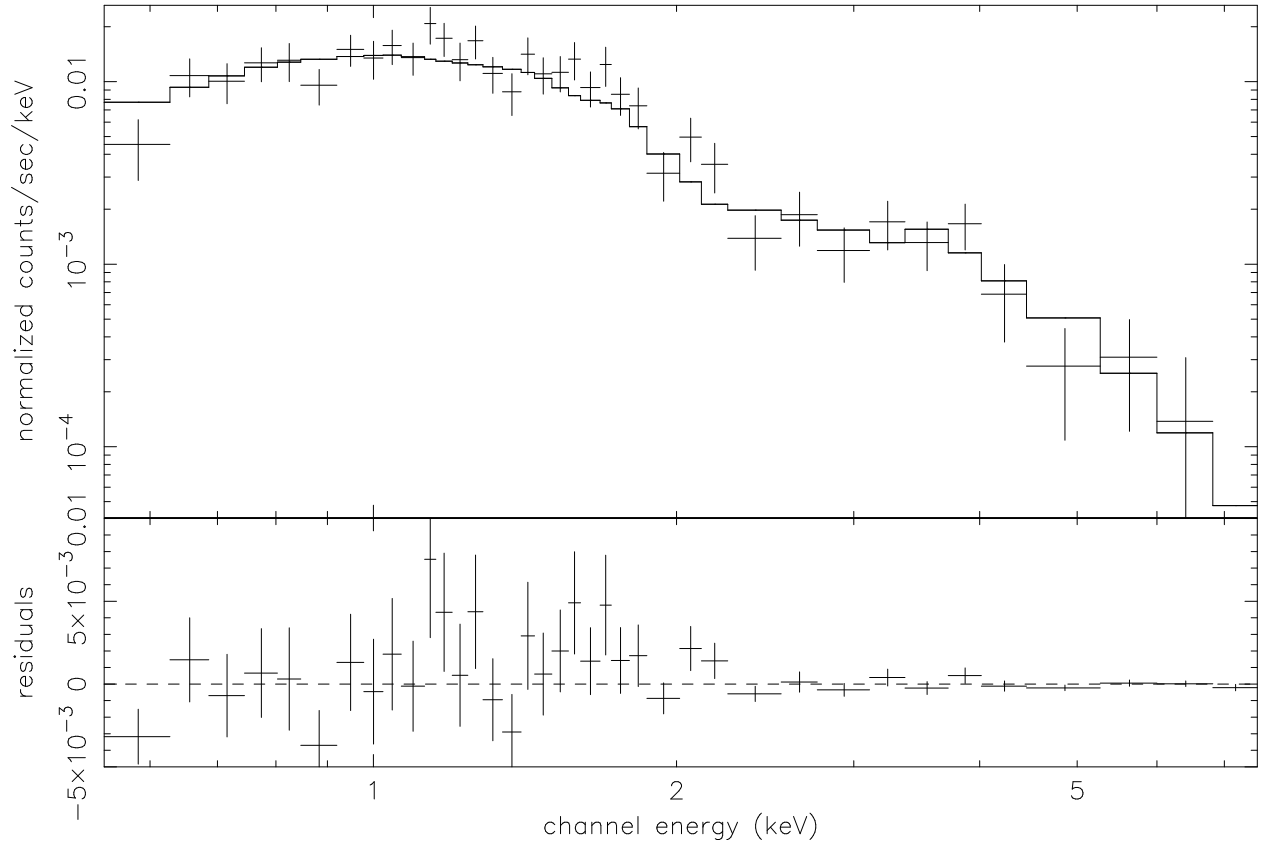


Fig. 7.— Spectrum and best-fit model of the northern subcluster of ClJ0152.7–1357.

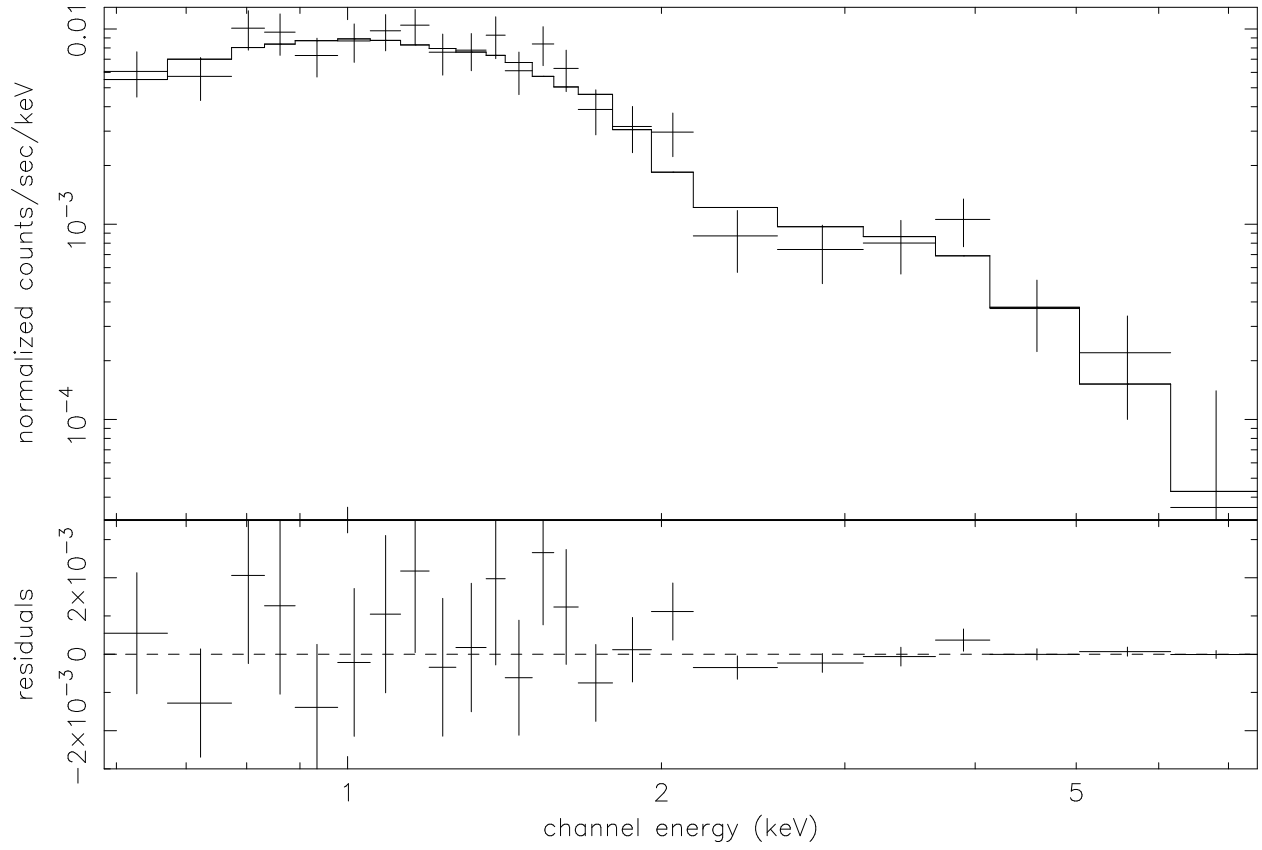


Fig. 8.— Spectrum and best-fit model of the southern subcluster of ClJ0152.7–1357.

The spectral fits yielded a temperature of $5.6_{-0.8}^{+1.0}$ keV, and an abundance of $0.15_{-0.15}^{+0.22}$ solar, with a reduced χ^2 value of 0.9 (36 degrees of freedom) for the northern subcluster. The southern subcluster was found to be slightly, but not significantly, cooler at a temperature of $4.8_{-0.9}^{+1.4}$ keV with a metal abundance of $0.70_{-0.44}^{+0.72}$ solar; the reduced χ^2 was 0.7 (35 degrees of freedom). We note that the abundances are poorly constrained and so we prefer to fit for the temperature with the abundance frozen at 0.3 solar. This then yields best-fit values of $5.5_{-0.7}^{+0.9}$ keV and $5.2_{-0.9}^{+1.1}$ keV for the northern and southern subclusters respectively, without significant changes to the reduced χ^2 values.

ROSAT observations of this system gave a temperature estimate of $5.9_{-2.1}^{+4.4}$ keV (Ebeling et al. 2000), while an analysis of a *BeppoSAX* observation produced a temperature of $6.5_{-1.2}^{+1.7}$ keV and a metallicity of $0.53_{-0.24}^{+0.29}$ solar (Della Ceca et al. 2000). Finally, Joy et al. (2001) use Sunyaev-Zel’dovich effect imaging of the cluster to estimate its ICM temperature at $8.5_{-1.5}^{+2.0}$ keV. While these quantities were all measured for the cluster as a whole, the X-ray temperatures are consistent with that of either subcluster as measured with *Chandra*. The *BeppoSAX* metallicity is in good agreement with that of the southern cluster and consistent with that of the northern subcluster, which is not surprising given the size of the 1σ errors of the measurements. The Sunyaev-Zel’dovich temperature estimate is higher than that of the *Chandra* temperature measurement, though at less than 2σ .

4.2. Spatial results

The spatial distribution of the X-ray emission of ClJ0152.7–1357 was examined as described in section 2.2. The system was modelled with two 2D β -profiles (one for each subcluster) and a constant background flux of 3.37×10^{-10} counts $\text{cm}^{-2} \text{s}^{-1}$ as estimated from an independent 2D fit to a background region of the same CCD. Five point sources in the fitting regions were masked out, and the model was fit to the data in Sherpa, using a maximum-likelihood algorithm and the C statistic. The best-fit parameter values for the northern subcluster were $r_c = 32.7_{-4.3}^{+8.3}''$ (248_{-33}^{+63} kpc), $\beta = 0.73_{-0.06}^{+0.13}$, and $e = 0.08$. The fit to the southern subcluster yielded $r_c = 16.1_{-2.6}^{+3.7}''$ (122_{-20}^{+28} kpc), $\beta = 0.66_{-0.06}^{+0.08}$, and $e = 0.00$. Errors were computed with all parameters free to vary.

Radial profiles of the X-ray surface brightness were then produced for each subcluster. In both cases the profiles were extracted from a semi-circular region spanning 180° away from the direction of the merger to avoid contamination by the emission from the other subcluster. The radial bins were adaptively sized so that their minimum width was 2 pixels ($\approx 1''$) and the minimal snr value per bin was 3. In the case of the northern subcluster, emission was detected out to $85''$ at this level; in the case of the southern subcluster, the

detection extended to $90''$. These radii are in good agreement with the size of the 2D fitting region. For the northern subcluster a best-fitting radial profile was obtained for $r_c = 33_{-8}^{+12}''$ (251_{-61}^{+91} kpc) and $\beta = 0.74_{-0.13}^{+0.23}$, with a reduced χ^2 value of 0.7 (28 degrees of freedom). This fit agrees well with the one derived from the best-fitting 2D model; the data and best-fitting 1D model are shown in Fig. 9. The best-fitting model to the southern profile is parameterised by $r_c = 11.6_{-2.6}^{+3.2}''$ (88_{-20}^{+24} kpc) and $\beta = 0.57_{-0.05}^{+0.07}$, with a reduced χ^2 value of 0.4 (17 degrees of freedom); data and model are shown in Fig. 10. These values are lower than those found with the 2D fitting, but not significantly so. In only considering half of the emission from each subcluster the errors, already large due to poor photon statistics, are increased further, leading to yet greater uncertainties in the 1D fit results and low χ^2 values. 2D fitting seems to be the best approach to model this complex system as the emission from both subclusters can be fit simultaneously, thus making the most of the available photons. This method also has the advantage that any excess emission over that expected from two clusters overlapping in projection will be apparent in the residuals of the fit.

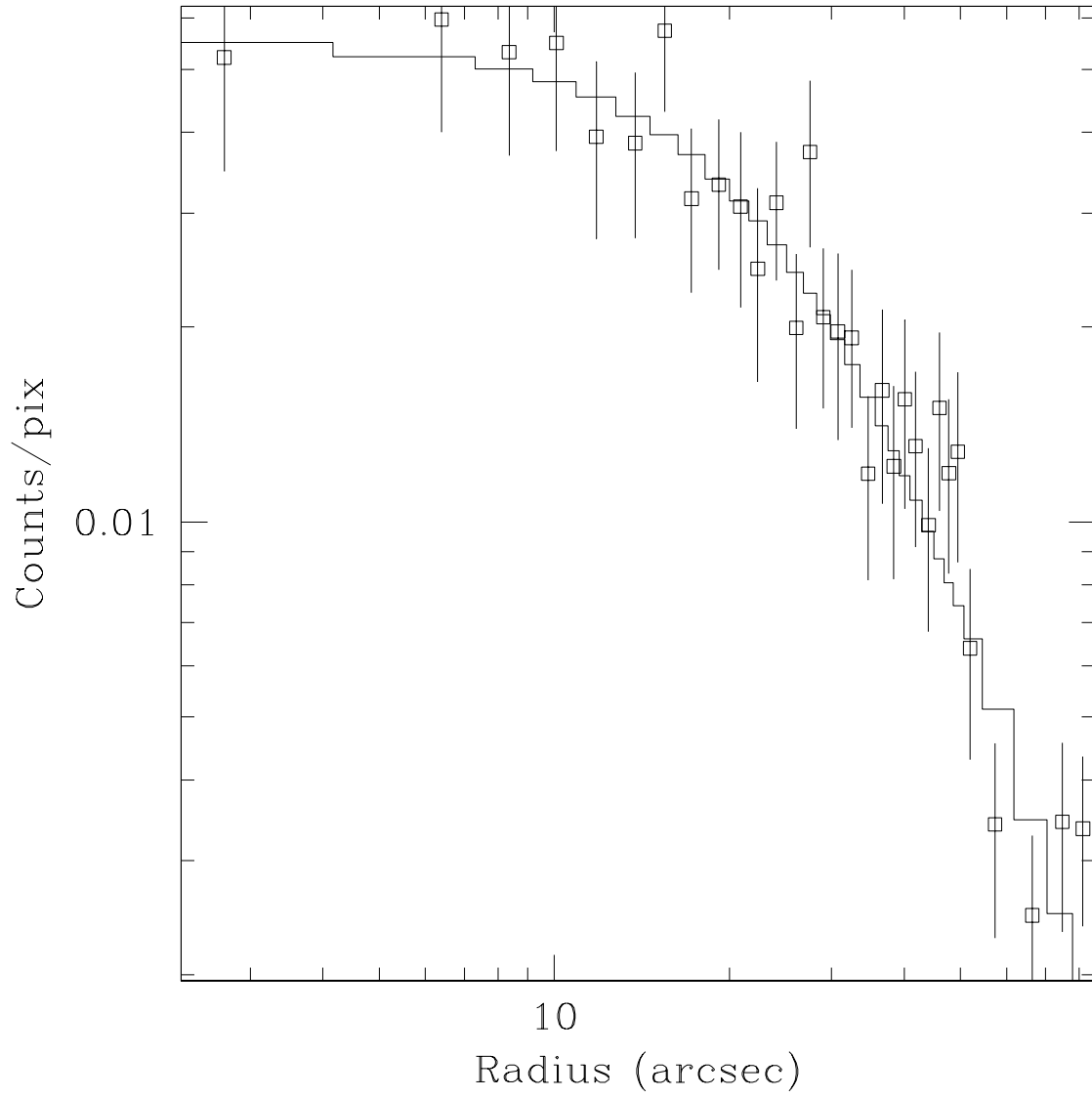


Fig. 9.— X-ray surface brightness profile of the northern subcluster of CLJ0152.7–1357 in a semi-circular region spanning 180° away from the direction of the merger. The line shows the best-fit 1D β -model.

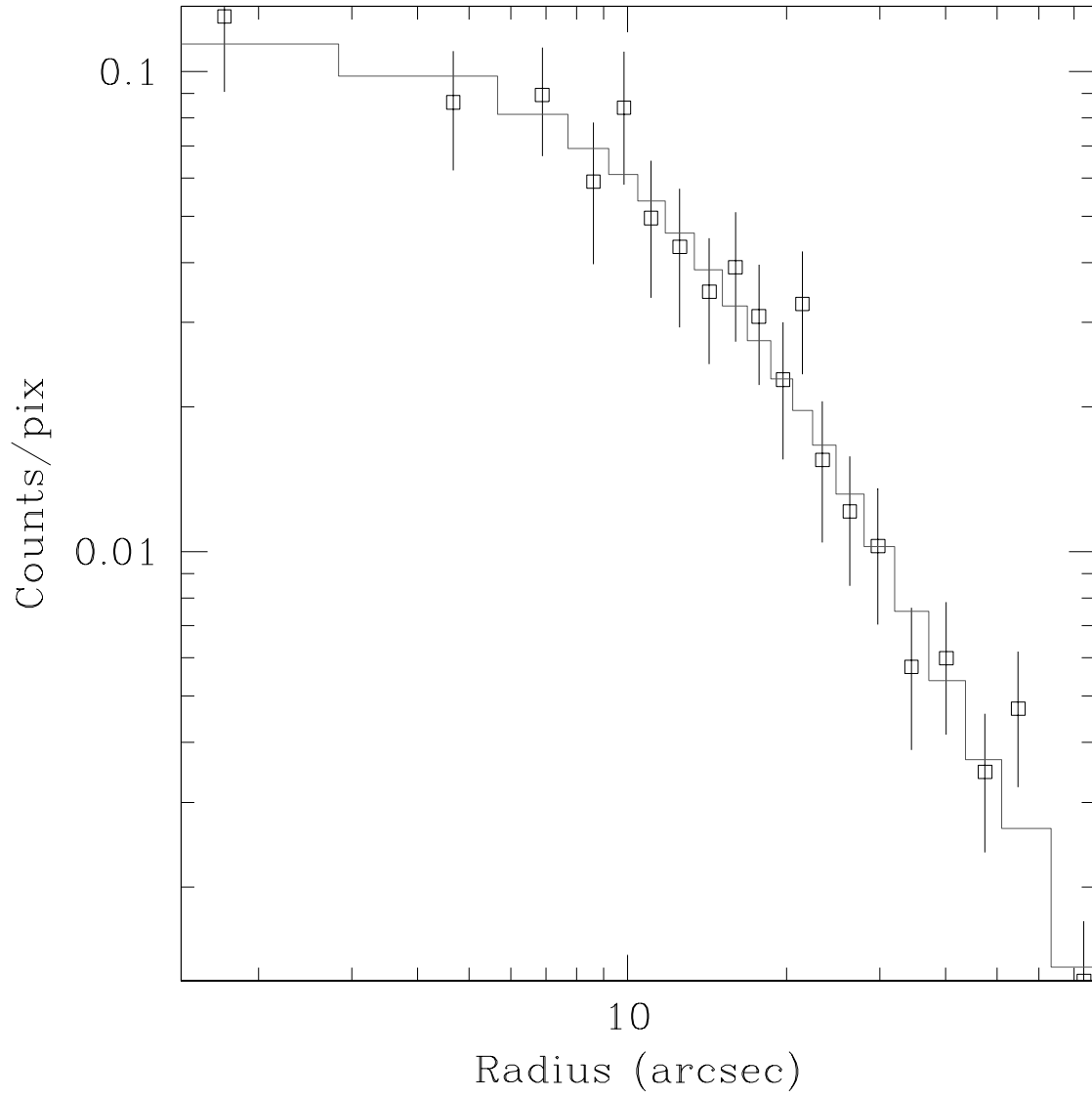


Fig. 10.— X-ray surface brightness profile of the southern subcluster of CLJ0152.7–1357 in a semi-circular region spanning 180° away from the direction of the merger. The line shows the best-fit 1D β -model.

A residual map was produced by subtracting the best-fit model (convolved with the PSF and multiplied by the exposure map) from the data, and then smoothing the resulting image with a Gaussian kernel of size $\sigma = 3''$. Contours of the positive residuals are shown in Fig. 11, overlaid on a hardness ratio map of the cluster emission, produced using the regions of excess emission as a guide. The hardness ratios of the emission were calculated as described in section 3.1. Immediately apparent is a linear feature of excess emission between the two subclusters, oriented perpendicular to their merger axis. This narrow feature (width $< 5''$) is suggestive of a shock front between the merging subclusters. It is, however, significant at only the 4.2σ level, in a region carefully chosen to maximise its significance (the rectangle in Fig. 11; note that this region excludes a point source at the western end of the feature). This region also has harder emission than either of the subclusters, corresponding to hotter gas (see Table 1), as one would expect in a region of compression, though this result is not strongly significant. If confirmed, this feature would constitute the first direct detection of a shock in the early stages of a cluster merger. No other systematic residuals are apparent in the outer cluster regions, indicating that, overall, our model fits the data well.

Additional residuals of excess emission are, however, observed in the core of each subcluster (regions C and F in Fig. 11), suggesting the possible presence of cooling flows (*e.g.* Fabian 1994), but these residuals are significant at only the 3σ level. The core of the northern subcluster may have the softest emission in this system (but the errors are large), consistent with a cooling flow, but the opposite is the case in the southern subcluster. Simulations predict that cooling flows are disrupted in the late stages of major mergers such as this one (Ritchie & Thomas 2002). The possible existence of at least one cool cluster core in this developing merger suggests that the central regions of the approaching systems are still fairly undisturbed and likely close to hydrostatic equilibrium.

Table 1. Values of the hardness ratios, and corresponding temperatures measured for the regions shown in Fig. 11

Region	Hardness ratio	Temperature (keV)
A	0.82 ± 0.08	$8.8_{-2.0}^{+2.6}$
B	0.58 ± 0.11	$4.4_{-1.1}^{+1.5}$
C	1.24 ± 0.29	> 14.1
D	0.68 ± 0.10	$5.7_{-1.3}^{+2.0}$
E	0.78 ± 0.14	$7.7_{-2.6}^{+4.8}$

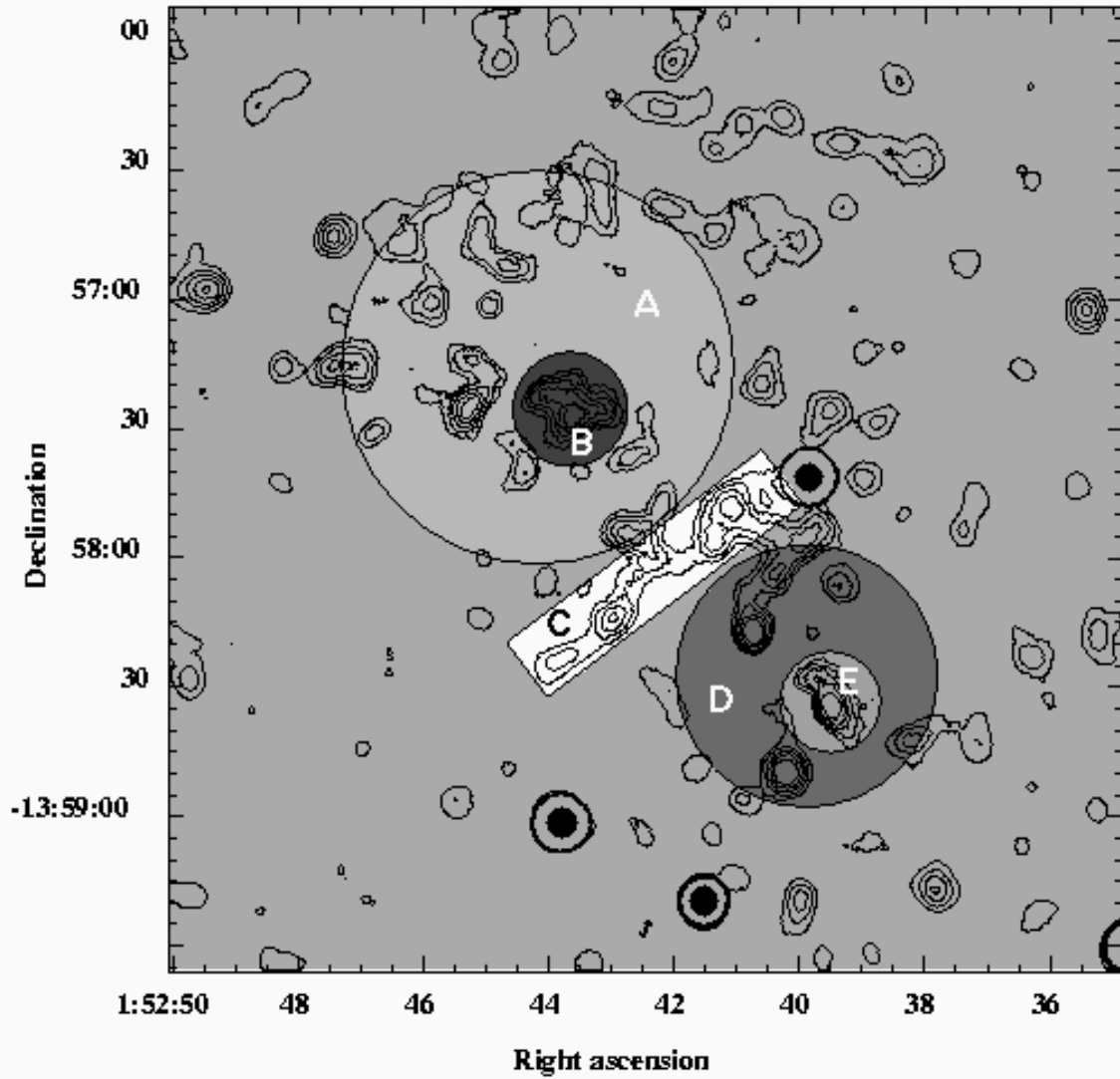


Fig. 11.— Hardness ratio map of ClJ0152.7–1357, overlaid with contours of excess X-ray emission above the best-fitting surface brightness model. Lighter colours represent harder emission; the values for each region are given in Table 1. Note that the three point sources which appear black were excluded from this analysis

Using Eqn. 5 the virial radius of the northern subcluster is estimated to be 1.4 ± 0.1 Mpc. The spectral radius used in our analysis thus corresponds to approximately $0.27 r_v$. For the southern cluster we find our spectral radius to reach about 20% of the virial radius of $r_v = 1.4 \pm 0.1$ Mpc.

Cluster fluxes for the two cluster components were initially measured within the respective spectral radii, and then, as before, scaled out to the virial radius by integrating the respective best-fit surface brightness model to yield approximate total fluxes. The unabsorbed total fluxes were used to estimate the luminosities of the subclusters. For the northern subcluster we find a bolometric luminosity of $L(r_v) = 1.0 \pm 0.2 \times 10^{45}$ erg s⁻¹; for the southern subcluster the corresponding value is $L(r_v) = 5.8_{-0.9}^{+1.2} \times 10^{44}$ erg s⁻¹. Combined, these values lead to a total bolometric luminosity of ClJ0152.7–1357 of $L(r_v) = 1.6 \pm 0.2 \times 10^{45}$ erg s⁻¹.

The subcluster fluxes measured in the 0.5 – 2 keV band, again extrapolated to r_v , were combined to estimate the total flux of ClJ0152.7–1357 in this band for comparison with earlier measurements, adopting the Einstein-de Sitter cosmology. We find $F(r_v) = 1.83_{-0.18}^{+0.22} \times 10^{-13}$ erg s⁻¹ cm⁻², slightly lower than the value of $2.9_{-0.18}^{+0.18} \times 10^{-13}$ erg s⁻¹ cm⁻² measured from the *ROSAT* data (Ebeling et al. 2000). The higher value found in the *ROSAT* data could be explained by a contribution from point sources which were unresolved by that instrument, but which are excluded here, and by the fact that the *Chandra* flux is extrapolated out to the virial radius, rather than to infinity. For completeness’ sake we also computed the bolometric luminosity of each subcluster in our alternative, Einstein-de Sitter cosmology (see Table 3). The total bolometric luminosity of ClJ0152.7–1357 (both subclusters combined) is $L(r_v) = 1.81_{-0.18}^{+0.21} \times 10^{45}$ erg s⁻¹ in this cosmology, in good agreement with the value of $2.2_{-0.5}^{+0.5} \times 10^{45}$ erg s⁻¹ derived from the *BeppoSAX* observation (Della Ceca et al. 2000).

Following the procedure detailed in section 2, the central gas densities, gas masses, total gravitating masses, and gas mass fractions of each subcluster were computed, with results as listed in Table 2 and Table 3 for the two different cosmologies. We confirm that ClJ0152.7–1357 is indeed a massive cluster; the combined total mass of the two subclusters extrapolated to the virial radius is $1.1 \pm 0.2 \times 10^{15} M_\odot$ (Λ CDM cosmology).

The Sunyaev-Zel’dovich effect (SZE) work of Joy et al. (2001) quotes an estimate of the mass of ClJ0152.7–1357 of $\gtrsim 2 \times 10^{14} h_{100}^{-1} M_\odot$, within a single radius of 65" for the entire system. While the different geometry used by Joy et al. (2001) prohibits a direct comparison of their estimate with the masses derived here, we note that the masses of the subclusters within the spectral radii ($\sim 50''$) combine to give $2.4_{-0.3}^{+0.4} \times 10^{14} h_{70}^{-1} M_\odot$ in good agreement with the SZE estimate.

4.3. Cluster dynamics

We now attempt to address the question of whether ClJ0152.7–1357 is a gravitationally bound system. The redshifts of nine member galaxies in each subcluster have been measured (Demarco et al. 2002), allowing us to ascribe mean redshifts of $z = 0.8352 \pm 0.0017$ and $z = 0.8294 \pm 0.0013$ to the northern and southern subclusters respectively. Via the relativistic redshift equation

$$\frac{v}{c} = \frac{(z + 1)^2 - 1}{(z + 1)^2 + 1} \quad (10)$$

the difference between these redshifts can be translated into a line-of-sight velocity difference between the subclusters of $\Delta v = 660 \pm 258 \text{ km s}^{-1}$. This non-vanishing value of Δv can be caused by two effects:

- The subclusters are separated by the difference in the (line-of-sight) distances implied by their redshifts, i.e. 58 Mpc, and are being carried apart by the differential of the Hubble flow at these distances.
- The subclusters are at approximately the same distance, and Δv is a peculiar velocity reflecting the merger process.

The former case implies a chance superposition of two separate clusters, which can be regarded as extremely unlikely because the high mass and temperature of the two subclusters makes them very rare objects indeed. In the following we assess the probability of the second scenario, which implies that the system is gravitationally bound, using the system’s observed properties and the technique described by Hughes et al. (1996).

Given a line-of-sight velocity difference v_r and a projected separation R_p between the two subclusters of ClJ0152.7–1357, the true peculiar velocity v and separation R can be written as

$$v_r = v \cos \Psi_v \quad (11)$$

$$R_p = R \sin \Psi_R, \quad (12)$$

where Ψ_v and Ψ_R are the inclination angles of the velocity and separation vectors, respectively. Note that different values of Ψ_v and Ψ_R imply an orbital component in addition to the radial component of the relative motion of the subclusters. The system is bound when the kinetic energy of the subclusters is less than the gravitational potential of the system, a condition that can be expressed as

$$v_r^2 - \frac{2GM}{R_p} \sin \Psi_R \cos^2 \Psi_v < 0, \quad (13)$$

where M is the total mass of the system. The values of the relevant quantities, for the CLJ0152.7–1357 system, are $R_p = 722$ kpc, $v_r = 660$ km s⁻¹ and $M = 1.13 \times 10^{15} M_\odot$.

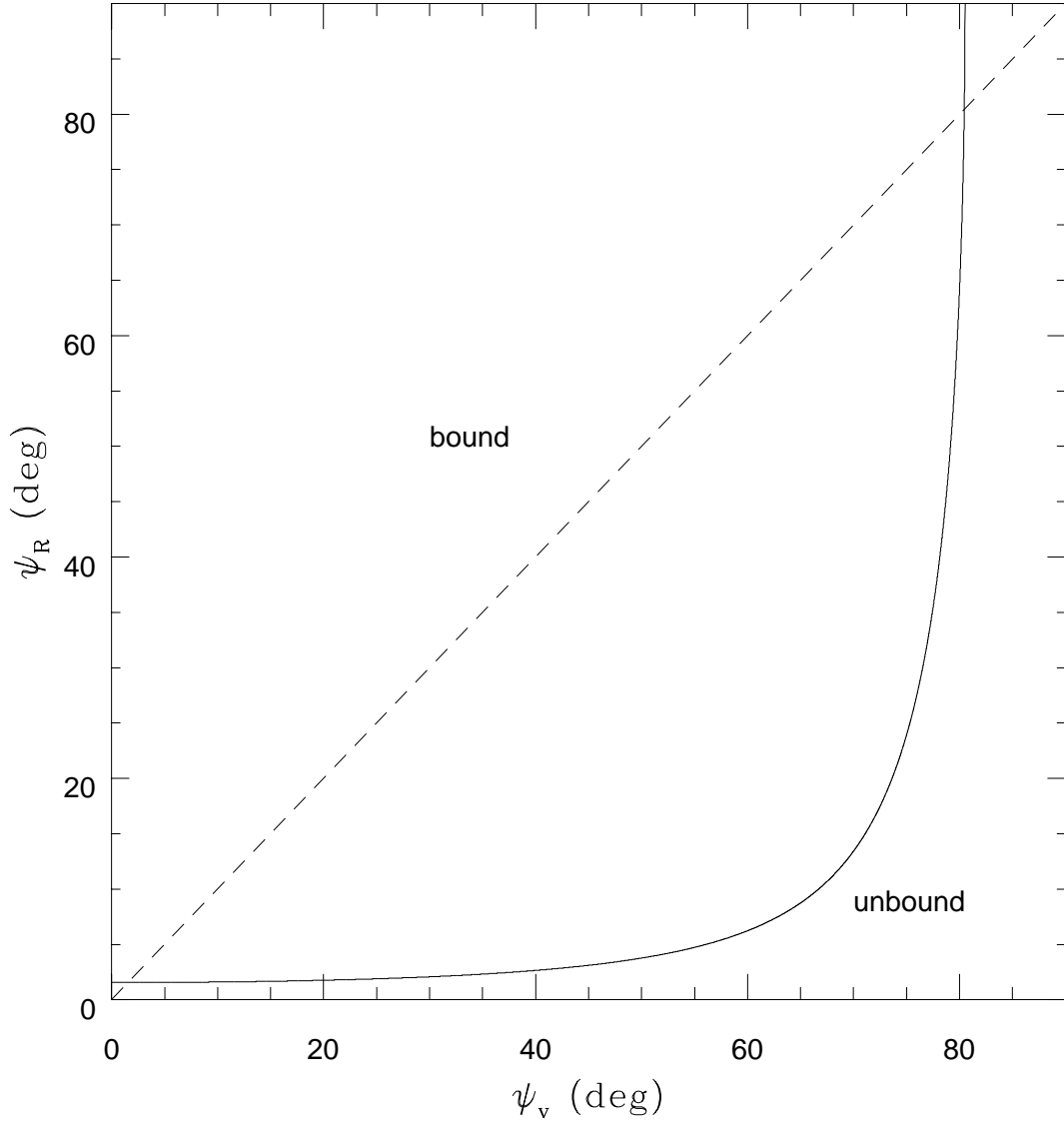


Fig. 12.— Regions of the (Ψ_v, Ψ_R) plane corresponding to the bound and unbound solutions of Eqn. 13 for the ClJ0152.7–1357 system. The dashed line is equivalent to a purely radial motion of the subclusters.

Fig. 12 shows the regions of the (Ψ_v, Ψ_R) plane corresponding to the bound and unbound solutions of Eqn. 13. The likelihood that the system is bound equals the probability of the projection angles having the appropriate values to place the system in the bound region of the (Ψ_v, Ψ_R) plane. This probability is given by the ratio of the solid angle through which a given projection angle is observable, to the solid angle of a sphere. Hence the probability that Ψ_R has a value in the range Ψ_R to $\Psi_R + \Delta\Psi_R$ is given by

$$P(\Psi_R) = \int_{\Psi_R}^{\Psi_R + \Delta\Psi_R} \frac{2\pi \cos \Psi_R}{4\pi} d\Psi_R. \quad (14)$$

The overall probability that the system is bound can then be obtained as the sum of the probabilities of the different combinations of projection angles in the bound region of the (Ψ_v, Ψ_R) plane. Without constraints on the range of permissible angles, we find the probability that the system ClJ0152.7–1357 is gravitationally bound, to be 0.78.

5. Discussion

The measured and derived properties of ClJ1113.1–2615 and ClJ0152.7–1357 are summarised in Table 2, with the properties of ClJ0152.7–1357 given for both the individual subclusters and for the cluster as a whole, where appropriate. Cluster properties derived using our alternative Einstein-de Sitter cosmology are summarised in Table 3.

Table 2. Summary of the measured and inferred properties of the galaxy clusters ClJ1113.1–2615 and ClJ0152.7–1357, based on the *Chandra* observations discussed here and assuming a Λ CDM cosmology of $\Omega_M = 0.3$ ($\Omega_\Lambda = 0.7$) and $H_0 = 70 \text{ km s}^{-1} \text{ Mpc}^{-1}$. Where appropriate, the properties of ClJ0152.7–1357 are listed for both the northern (ClJ0152.7–1357N) and southern (ClJ0152.7–1357S) subclusters individually, as well as for the cluster as a whole. The temperatures quoted were derived from spectral fits with abundances frozen at 0.3 solar.

Cluster	Redshift	$T(\text{keV})$	$L_{bol}(\text{erg s}^{-1})^a$	$r_c(\prime\prime)$	β	e	$r_v(\text{Mpc})$	$M_g(r_v)(M_\odot)$	$M(r_v)(M_\odot)$	$M_g/M(r_s)$	$M_g/M(r_v)$
ClJ1113.1–2615	0.725	$4.3^{+0.5}_{-0.4}$	$3.3^{+0.3}_{-0.3} \times 10^{44}$	$14.6^{+1.2}_{-2.2}$	$0.67^{+0.03}_{-0.05}$	0.2	1.3 ± 0.1	$3.0^{+0.4}_{-0.4} \times 10^{13}$	$4.3^{+0.8}_{-0.7} \times 10^{14}$	$0.05^{+0.01}_{-0.01}$	$0.07^{+0.01}_{-0.01}$
ClJ0152.7–1357S	0.833	$5.2^{+1.1}_{-0.9}$	$5.8^{+1.1}_{-0.9} \times 10^{44}$	$16.1^{+3.7}_{-2.6}$	$0.66^{+0.08}_{-0.06}$	0.00	1.4 ± 0.1	$4.5^{+1.3}_{-1.1} \times 10^{13}$	$5.2^{+1.8}_{-1.4} \times 10^{14}$	$0.06^{+0.02}_{-0.01}$	$0.09^{+0.04}_{-0.03}$
ClJ0152.7–1357N	0.833	$5.5^{+0.9}_{-0.8}$	$1.0 \pm 0.2 \times 10^{45}$	$32.7^{+8.3}_{-4.3}$	$0.73^{+0.13}_{-0.06}$	0.08	1.4 ± 0.1	$7.0^{+1.7}_{-1.5} \times 10^{13}$	$6.1^{+1.7}_{-1.5} \times 10^{14}$	$0.09^{+0.02}_{-0.01}$	0.12 ± 0.04
ClJ0152.7–1357	0.833		$1.6 \pm 0.2 \times 10^{45}$						$1.1 \pm 0.2 \times 10^{15}$		

^aBolometric luminosity computed from fluxes scaled out to the virial radius.

Table 3. As for Table 2, but assuming an Einstein-de Sitter cosmology of $H_0 = 50 \text{ km s}^{-1} \text{ Mpc}^{-1}$ and $\Omega_M = 1$ ($q_0 = 0.5$).

Cluster	$F(r_v)(0.5 - 2 \text{ keV}) \text{ erg s}^{-1} \text{ cm}^{-2}$	$L_{bol}(\text{erg s}^{-1})^a$	$r_v(\text{Mpc})$	$M_g(r_v)(M_\odot)$	$M(r_v)(M_\odot)$	$M_g/M(r_s)$	$M_g/M(r_v)$
ClJ1113.1–2615	$5.7 \pm 0.5 \times 10^{-14}$	$3.9^{+0.4}_{-0.3} \times 10^{44}$	1.1 ± 0.1	$2.8^{+0.4}_{-0.3} \times 10^{13}$	$3.6^{+0.7}_{-0.6} \times 10^{14}$	0.06 ± 0.01	0.08 ± 0.01
ClJ0152.7–1357S	$6.9^{+1.3}_{-1.0} \times 10^{-14}$	$6.7^{+1.2}_{-0.9} \times 10^{44}$	1.1 ± 0.1	$4.0^{+1.0}_{-0.8} \times 10^{13}$	$4.3^{+1.5}_{-1.2} \times 10^{14}$	$0.06^{+0.02}_{-0.01}$	$0.09^{+0.04}_{-0.03}$
ClJ0152.7–1357N	$1.1 \pm 0.2 \times 10^{-13}$	$1.1 \pm 0.2 \times 10^{45}$	1.2 ± 0.1	$6.3^{+1.3}_{-1.1} \times 10^{13}$	$5.0^{+1.4}_{-1.2} \times 10^{14}$	0.10 ± 0.02	0.13 ± 0.04
ClJ0152.7–1357	$1.8 \pm 0.2 \times 10^{-13}$	$1.8 \pm 0.2 \times 10^{45}$			$9.3^{+2.1}_{-1.7} \times 10^{14}$		

^aBolometric luminosity computed from fluxes scaled out to the virial radius.

We find ClJ1113.1–2615 to be a relaxed, hot and massive cluster at $z = 0.725$. The lack of pronounced substructure suggests that we are observing this system some time after its formation, or any recent mergers. On the other hand, the small but non-zero ellipticity of the X-ray emission may be interpreted as a remnant of the last merger event.

ClJ0152.7–1357 is found to be a very massive, hot system at $z = 0.833$, which consists of two massive subclusters that are likely in the process of merging. This scenario is supported by our dynamical analysis of the system, which shows that the subclusters are likely to be gravitationally bound, the X-ray contours, which show extensions away from the hypothesised direction of the merger, and a displacement between the viscous ICM and the essentially collisionless galaxies of the southern subcluster, which suggests a motion of this subcluster in a northerly direction toward the northern subcluster. It is difficult to compare this observation with recent detailed simulations of cluster mergers as they do not generally include galaxies.

Excess X-ray emission suggestive of a shock front is detected between the subclusters. Numerical simulations of equal-mass mergers (*e.g.* Roettiger et al. 1996; Ritchie & Thomas 2002) show the formation of such a shock front in the early stages of the merging process as the outer regions of the subclusters meet and gas is driven out perpendicular to the merger axis. The gas in the shocked region is further compressed and heated as the merger continues, becoming detectable by its increased density and temperature. The emission detected from the shock region in ClJ0152.7–1357 is harder than the surrounding emission, which is also consistent with the shock front scenario. The overall evidence is suggestive of a weak shock front in this merging system, although the limited number of photons prevent a robust detection. Future, deeper X-ray observations are needed to clarify the situation.

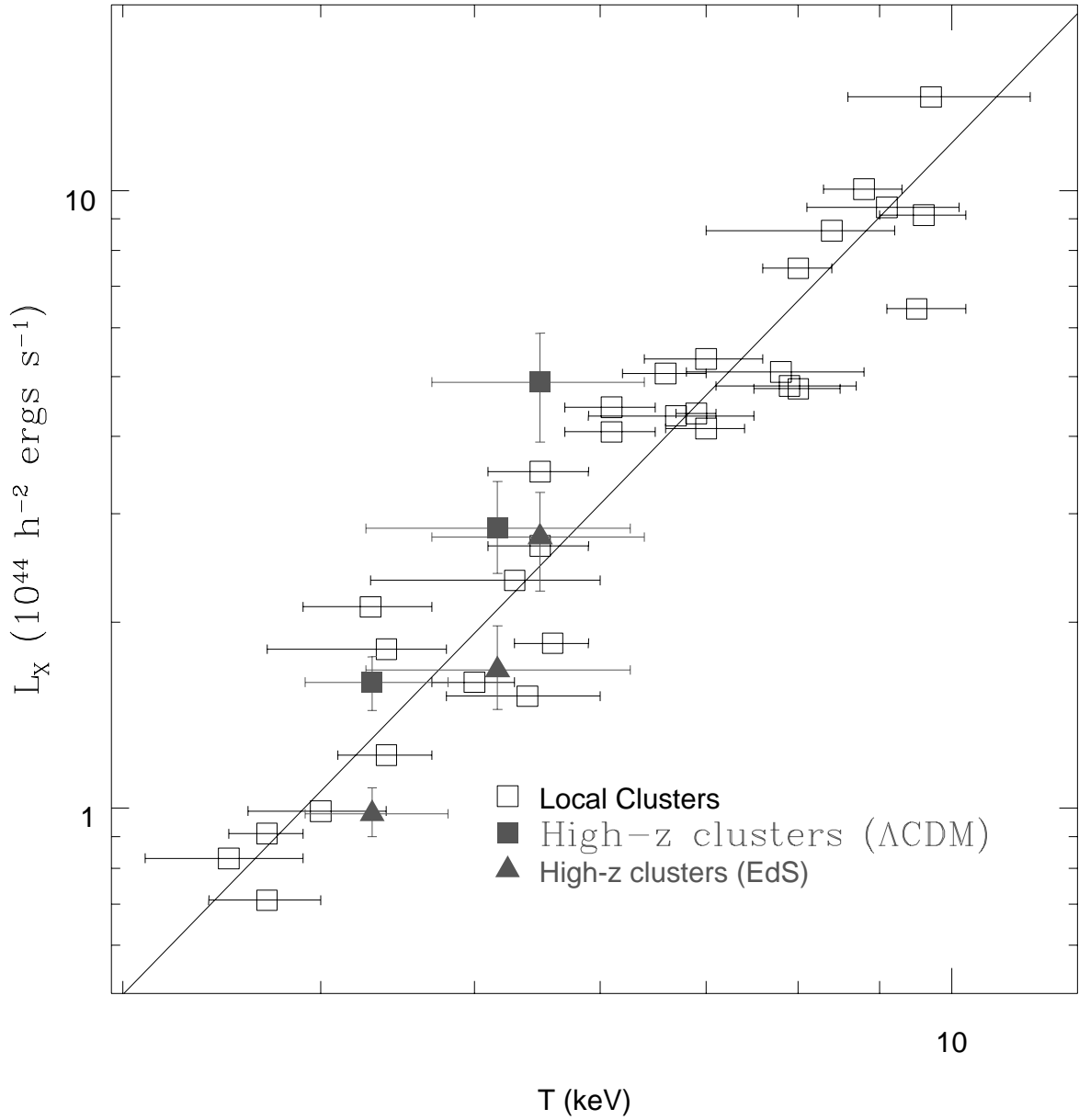


Fig. 13.— Bolometric X-ray luminosities and temperatures of the clusters analysed here are plotted on the low-redshift L-T relation of Markevitch (1998) in our two cosmologies. Our new data points are shown as filled squares (Λ CDM) and filled triangles (Einstein-de Sitter), and represent, from left to right, ClJ1113.1–2615, ClJ0152.7–1357S, and ClJ0152.7–1357N.

5.1. Evolution of cluster scaling relations

We now compare the X-ray properties of the three clusters analysed here (we here treat the two subclusters of ClJ0152.7–1357 separately) to those expected based on low- z scaling relations. We first examine the luminosity-temperature (L-T) relation, using the temperatures and luminosities of Markevitch (1998) corrected for cooling flow contamination, which should be consistent with the quantities we measure, as the high-redshift systems do not appear to host strong cooling flows. The luminosities were derived in our two model cosmologies, and are shown in Fig. 13. Previous work, assuming an Einstein-de Sitter cosmology has tended to find little, or no evolution in the L-T relation (*e.g.* Fairley et al. 2000), and our new data support this; the Einstein-de Sitter points are consistent with the local L-T relation. This indicates that contamination by unresolved point sources of observations made with earlier satellites (*e.g.* by Fairley *et al.*) was not, on average, a very significant effect. Recent work, assuming a Λ CDM cosmology has found evidence for positive evolution of the L-T relation (*e.g.* Arnaud et al. 2002b; Vikhlinin et al. 2002), *i.e.* clusters at high redshift are more luminous for a given temperature (although Holden et al. (2002) find no significant evolution in this cosmology). Our data support this general trend of positive evolution, albeit with low statistical significance, due to the few points available.

The loci of our three clusters were also plotted on the low-redshift β -T relation of Sanderson et al. (2002) (Fig. 14), which covers redshifts out to $z \sim 0.1$. Our three data points lie within the scatter around the β -T relation, suggesting again that the clusters we observe at redshifts $z \approx 0.8$ have a similar distribution of gas to that of systems in the local universe.

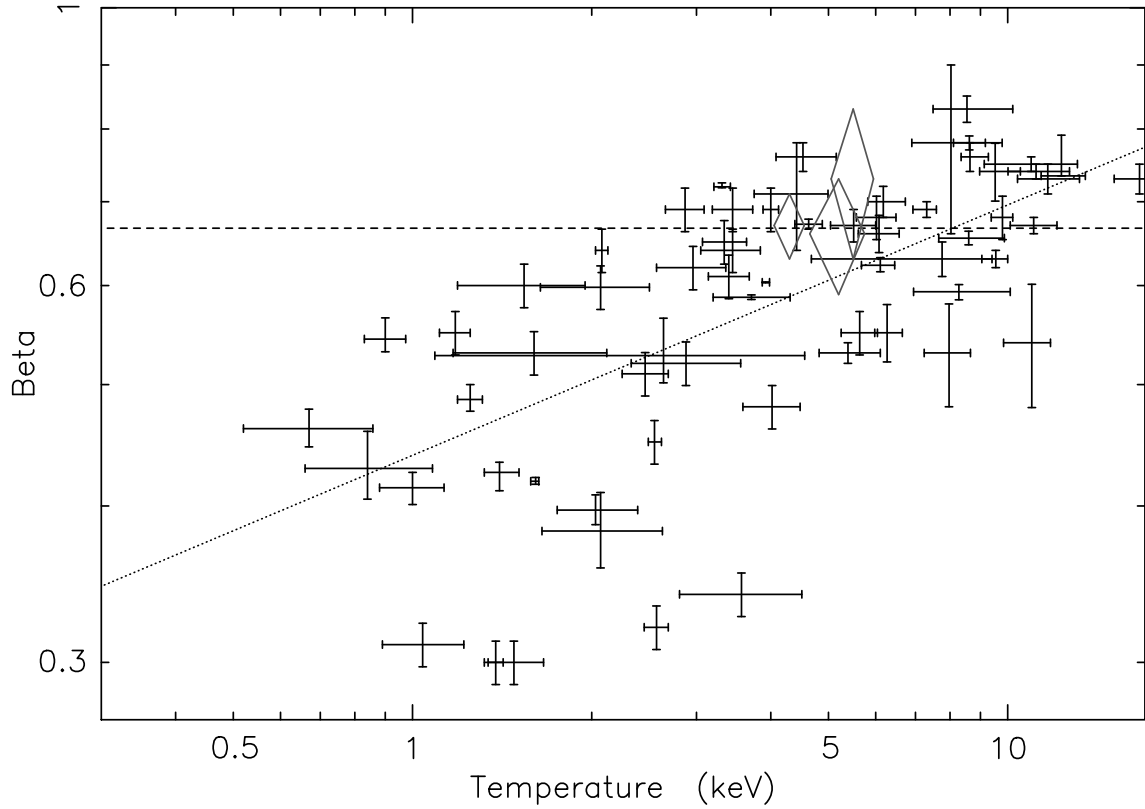


Fig. 14.— β values and temperatures of the clusters analysed here plotted on the low- z β – T relation of Sanderson et al. (2002). Our new data are shown as diamonds, and represent, from left to right, ClJ1113.1–2615, ClJ0152.7–1357S, and ClJ0152.7–1357N. The solid line shows the best fit to the low- z data, while the dashed line indicates the canonical value of $\beta = 2/3$.

The gas mass fractions of all three clusters were measured within their spectral radii, and total values were obtained by extrapolating to their virial radii. Note that, since the X-ray emission was only detected to 20 – 50% of the virial radii, only around 20% of the estimated total gas mass is directly observed. To allow a comparison of our results with those from the low-redshift study of Sanderson et al. (2002) who compute cluster gas mass fractions at $0.3r_v$, we also derived the gas mass fraction of our clusters at this radius (slightly larger than our spectral radii) in our Λ CDM cosmology (this is consistent with the values of $H_0 = 70 \text{ km s}^{-1} \text{ Mpc}^{-1}$ assumed by Sanderson and coworkers). The results are plotted along with the data of Sanderson et al. (2002) in Fig. 15. The loci of our high-redshift clusters do not deviate significantly from the low redshift data, suggesting that, for this cosmology, the composition of at least some galaxy clusters does not change significantly from $z \sim 0.8$ to $z \sim 0.1$.

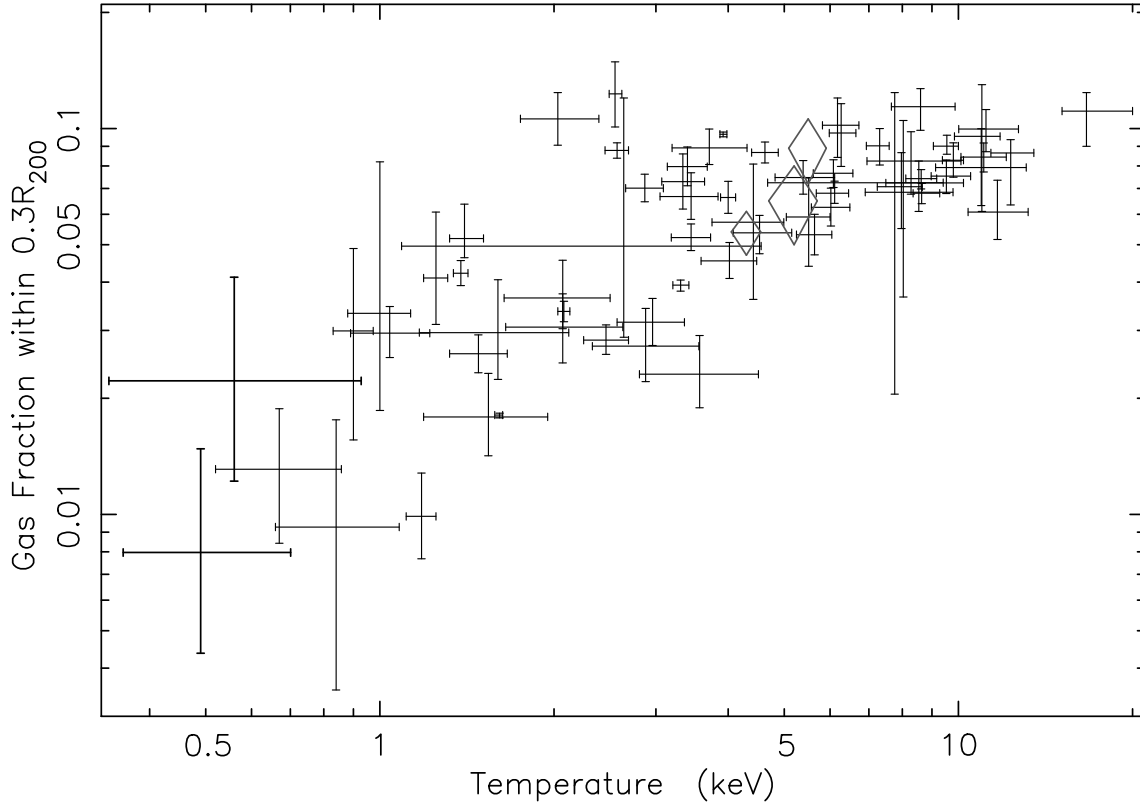


Fig. 15.— The loci of the three clusters observed by *Chandra* discussed here (diamonds) plotted on the gas-mass fraction versus temperature plot of Sanderson et al. (2002) for low-redshift clusters. For all clusters the gas-mass fraction was evaluated at $0.3r_v$. The new data points represent, from left to right, ClJ1113.1–2615, ClJ0152.7–1357S, and ClJ0152.7–1357N.

5.2. The M-T relation

Finally, we compare the mass-temperature relation found in the local sample of Sanderson et al. (2002) with the properties measured for our high-redshift clusters, and for the intermediate redshift sample of Allen et al. (2001). This intermediate redshift sample provides a useful comparison, as it has secure mass measurements within R_{2500} derived from *Chandra* temperature profiles, and corroborated by weak-lensing measurements. The temperatures derived by those authors are unaffected by the ACIS low energy QE degradation since the low energy absorption was a free parameter in their analysis (Allen et al. 2002).

Fig. 16 shows the mass (within R_{2500}) of the hotter ($T > 4$ keV) systems from the local sample plotted against their mass weighted temperatures (measured within $0.3R_{200}$). The line shows the best fitting power law to the local data points, of the form $M = A_{2500}T^\alpha$, with $A_{2500} = 6.2_{-1.4}^{+1.7} \times 10^{12}M_\odot$ and $\alpha = 1.94 \pm 0.12$. The intermediate-redshift clusters (marked as barred crosses) have their mass (within R_{2500}) plotted against their mass weighted temperatures (also measured within R_{2500}). Finally, our new high-redshift data are plotted as diamonds, and we plot mass within $0.3R_{200}$ against emission-weighted temperatures (under our assumption of isothermality, the emission weighted temperature is the same as the mass weighted temperature, and constant with radius, though the errors quoted do not include any systematic uncertainties in the masses due to this assumption). Note that $0.3R_{200}$ is very close to R_{2500} (*e.g.* Sanderson et al. 2002), so the different scales used are consistent.

The most important result is that little or no evolution of the M-T relation is observed. In order to investigate quantitatively the evolution in the M-T relation we measured the mean offsets in mass of the high-redshift points, weighted by their errors, from the local M-T relation. The mean offset factors, calculated for the intermediate, and high-redshift samples are given in Table 4. The errors quoted are the formal errors in the weighted mean, based on the scatter of the data. For both samples the mean offset is consistent with zero, a conclusion confirmed by reduced χ^2 (and corresponding probability) values of 0.40(0.75) and 0.46(0.84) for the intermediate and high-redshift samples respectively, when compared to the local M-T relation.

The normalisation of the M-T relation is, however, expected to be lower for objects which formed at higher redshifts, because objects which form in a denser universe will be hotter for a given mass ($T \propto M/R$). The evolution of the normalisation can be modelled by a redshift dependent factor. A cluster of a given mass forming at a redshift z will have a temperature given by $E(z)M \propto T^{3/2}$, where $E(z) = (1+z)\sqrt{(1+z\Omega_M + \Omega_\Lambda)/(1+z)^2 - \Omega_\Lambda)}$. If we assume that the redshift of observation (z_{obs}) is the same as the redshift of formation (z_f), we would expect the high-redshift clusters to lie below the local M-T relation by a mean factor $1/\overline{E(z)}$ also given in Table 4 (for a Λ CDM cosmology). In fact, increasing the

observed masses by factors of $E(z)$ would place them above the local M-T relation, but not very significantly so, given the reduced χ^2 (and probability) values of 0.62(0.71) and 3.29(0.02) for the intermediate and high-redshift $E(z)M$ samples, when again compared to the local M-T relation (given that the errors on the high-redshift sample are underestimates because of the assumption of isothermality).

If this lack of evolution in the normalisation of the M-T relation is confirmed by further high-redshift cluster observations, then one interpretation is that $z_{obs} \neq z_f$, but that clusters still reflect the conditions of the epoch at which they formed. In this case the normalisation of the local M-T relation corresponds to some mean redshift of formation of the local clusters. The fact that the higher redshift clusters lie on the same, or a similar, M-T relation suggests that their redshift of formation is similar to that of the local systems.

An alternative, and perhaps more realistic, interpretation would be that clusters continuously grow in mass, rather than forming in one major merger event identified with a formation epoch. In this case the properties of clusters more closely correspond to the epoch at which they are observed, and less evolution in the M-T relation is predicted (Voit 2000; Mathiesen 2001). A more detailed comparison awaits better data.

Table 4. Mean weighted fractional offset factors in mass (\overline{dM}) from the local M-T relation of the Sanderson et al. (2002) data above 4 keV, and the predicted offset, $1/\overline{E(z)}$, based on the assumption of a single redshift of formation for each cluster that is the same as the observation redshift. The local offset excludes AWM7, the point far below the relation at ≈ 5.8 keV.

Redshift Range	\overline{dM}	$1/\overline{E(z)}$
< 0.1	0.99 ± 0.03	
0.1 – 0.45	0.95 ± 0.05	0.85
0.72 – 0.83	1.03 ± 0.08	0.64

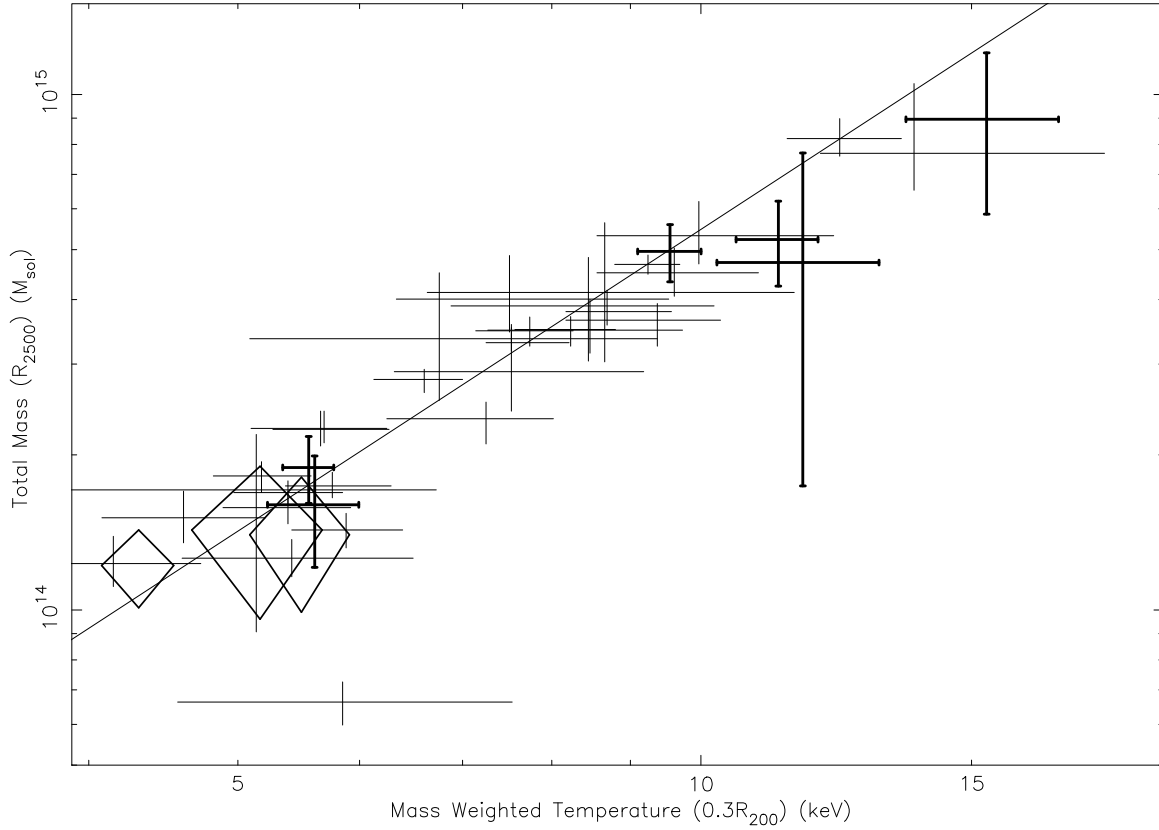


Fig. 16.— The loci of the three clusters analysed here are plotted as diamonds on the low- z $M - T$ relation of Sanderson et al. (2002). The solid line is the best fit to the local data at $T > 4$ keV and the heavy, barred crosses are from the Chandra data of intermediate-redshift clusters of Allen et al. (2001).

6. Conclusions

We have analysed *Chandra* X-ray observations of two massive high-redshift clusters of galaxies: CLJ1113.1–2615 ($z=0.725$) and ClJ0152.7–1357 ($z=0.833$). CLJ1113.1–2615 appears largely relaxed, whereas ClJ0152.7–1357 is likely to be in the early phase of an equal-mass merger of sufficient mass to create the Coma cluster; at 80% confidence the system is gravitationally bound.

Treating ClJ0152.7–1357 as two independent subclusters, we find the hot gas in the clusters studied to have very similar global properties to that in massive clusters at low redshift. The metallicity, gas fraction and gas density profile slope are all consistent with the values found in local clusters of similar temperature, suggesting that the gas was in place, and containing its metals, at $z = 0.8$. These properties point towards an early epoch of assembly of at least some massive clusters.

We measure the M-T relation at $z = 0.8$ for the first time, and find no significant evolution of the normalisation. This behaviour is more consistent with models in which clusters are continually evolving, rather than those in which each cluster reflects the conditions at a single formation epoch. It also supports the use of the X-ray temperature function at high redshifts to constrain cosmological parameters, especially Ω_m .

Finally, our data support the general consensus of little, or no evolution in the L-T relation under the assumption of an Einstein-de Sitter cosmology, and are consistent with recent suggestions of positive evolution in a Λ CDM cosmology.

7. Acknowledgements

We thank M. Arnaud and P. Thomas for useful discussions. LRJ acknowledges the UK PPARC for support during part of this work. BJM is supported by a PPARC postgraduate studentship. HE and EP gratefully acknowledge financial support from SAO grant GO0-1071A.

A. Effect of ACIS QE degradation on spectra

In this appendix we examine the effect of the ACIS QE degradation due to hydrocarbon contamination on the spectra analysed here, and the methods of correcting for this. There are currently three similar methods for correcting for the problem: The ACISABS model for XSPEC (<http://www.astro.psu.edu/users/chartas/xcontdir/>), the same model, implemented

for Sherpa (http://cxc.harvard.edu/ciao/threads/sherpa_acisabs/), and `corrarf`, a Fortran code that corrects the ARF using the ACISABS absorption model (http://cxc.harvard.edu/cal/Links/Acis/acis/Cal_prods/qeDeg/corrarf.tar.gz). All three methods use the same contamination rate, which has been derived from calibration observations, and assume the same composition of the contaminant.

We take the spectrum of ClJ1113.1–2615 as a test case, as this is the best quality spectrum of the three discussed here. The spectrum was fit with an absorbed MEKAL model, uncorrected, and with each of the three correction methods. As the contamination increases with time, the correction methods require the number of days between *Chandra* launch and the observation, to normalise the absorption. The observation of ClJ1113.1–2615 was taken 387 days after launch. The fits were performed in two energy ranges, 0.5 – 8 keV and 1 – 8 keV, and the column density was either frozen at the Galactic value, or allowed to fit. The best fitting temperatures and column densities are given in Table 5. The spectral parameters found for the three correction methods were completely consistent, so we just give those for XSPEC ACISABS for clarity. The MEKAL abundance was frozen at $0.3Z_{\odot}$ for simplicity.

Table 5. Best fitting spectral parameters with and without correcting for the *Chandra* low energy QE degradation. Hydrogen columns marked with (f) were frozen at the galactic value during the fit.

Correction	Range (keV)	nH (10^{22} cm $^{-2}$)	kT (keV)	Range (keV)	nH (10^{22} cm $^{-2}$)	kT (keV)
None	0.5 – 8 keV	0.054(f)	$5.2^{+0.7}_{-0.6}$	1 – 8 keV	0.054(f)	$4.7^{+0.6}_{-0.6}$
None	0.5 – 8 keV	$0.12^{+0.04}_{-0.04}$	$4.2^{+0.7}_{-0.6}$	1 – 8 keV	$0.062^{+0.142}_{-0.062}$	$4.7^{+0.7}_{-1.1}$
ACISABS	0.5 – 8 keV	0.054(f)	$4.4^{+0.7}_{-0.5}$	1 – 8 keV	0.054(f)	$4.4^{+0.6}_{-0.5}$
ACISABS	0.5 – 8 keV	$0.071^{+0.04}_{-0.04}$	$4.3^{+0.7}_{-0.7}$	1 – 8 keV	$0.054^{+0.109}_{-0.054}$	$4.4^{+0.8}_{-0.8}$

As the QE degradation is most severe below 1 keV we would expect the spectra fitted above this energy to give similar results, which is indeed the case. When the fit is extended below 1 keV, however, we find the the temperature is overestimated in the uncorrected spectra by $\approx 15\%$ when the absorbing column is fixed at the Galactic value. On the other hand, if the absorbing column is allowed to fit, the temperature found is generally accurate, while the absorption is significantly overestimated. It is reassuring, though, that all of the corrected spectral fits give consistent temperatures in both energy ranges, and agree well with the uncorrected spectra above 1 keV. The best fitting column densities given by the corrected spectral fits is also consistent with the Galactic value.

REFERENCES

- Allen, S. W., , Fabian, A. C., Schmidt, R. W., & H., E. 2002, astro-ph/0208394
- Allen, S. W., Schmidt, R. W., & Fabian, A. C. 2001, MNRAS, 328, L37
- Allen, S. W., Schmidt, R. W., & Fabian, A. C. 2002, MNRAS, 334, L11
- Arnaud, K. A. 1996, ASP Conf. Series, 101, 17
- Arnaud, M., Aghanim, N., & Neumann, D. M. 2002a, A&A, 389, 1A
- . 2002b, A&A, 390, 27A
- Birkinshaw, M., Hughes, J. P., & Arnaud, K. A. 1991, ApJ, 379, 466
- Borgani, S., Rosati, P., Tozzi, P., Stanford, S. A., Eisenhardt, P. R., Lidman, C., Holden, B., Della Ceca, R., Norman, C., & Squires, G. 2001, ApJ, 561, 13
- Cash, W. 1979, ApJ, 228, 939
- Cavaliere, A. & Fusco-Femiano, R. 1976, A&A, 49, L137
- Della Ceca, R., Scaramella, R., Gioia, I. M., Rosati, F., & Squires, G. 2000, A&A, 353, 498
- Demarco, R., Rosati, P., et al. 2002, A&A, in preparation
- Dickey, J. M. & Lockman, F. J. 1990, ARA&A, 28, 215
- Ebeling, H. 2002, MNRAS, submitted
- Ebeling, H., Jones, L. R., Perlman, E., Scharf, C., Horner, D., Wegner, G., Malkan, M., Fairley, B., & Mullis, C. R. 2000, ApJ, 534, 133

- Ettori, S., Tozzi, P., & Rosati, P. 2003, *A&A*, in press, (astro-ph/0211335)
- Evrard, A. E., Metzler, C. A., & Navarro, J. F. 1996, *ApJ*, 469, 494
- Fabian, A. C. 1994, *ARA&A*, 32, 277
- Fairley, B. W., Jones, L. R., Scharf, C., Ebeling, H., Perlman, E., Horner, D., Wegner, G., & Malkan, M. 2000, *MNRAS*, 315, 669
- Henry, J. P. 2000, *ApJ*, 533
- Henry, J. P. & Arnaud, K. A. 1991, *ApJ*, 372, 410
- Holden, B. P., Stanford, S. A., Squires, G. K., Rosati, P., Tozzi, P., Eisenhardt, P., & Spinrad, H. 2002, *ApJ*, 124, 33
- Hughes, J. P., Birkinshaw, M., & Huchra, J. P. 1996, *ApJ*, 448, L93
- Jones, L. R., Scharf, C., Ebeling, H., Perlman, E., Wegner, G., Malkan, M., & Horner, D. 1998, *ApJ*, 495, 100
- Joy, M., LaRoque, S., Grego, L., Carlstrom, J. E., Dawson, K., Ebeling, H., Holzappel, W. L., Nagai, D., & Reese, E. D. 2001, *ApJ*, 551, L1
- Kaastra, J. S. & Mewe, R. 1993, *aasupp*, 97, 443
- Liedahl, D. A., Osterheld, A. L., & Goldstein, W. H. 1995, *ApJ*, 438, L115
- Markevitch, M. 1998, *ApJ*, 504, 27
- . 2001, ACIS background (<http://hea-www.harvard.edu/maxim/axaf/acisbg/>)
- Markevitch, M., Gonzalez, L., Vikhlinin, A., Murray, S., Forman, W., Jones, C., & Tucker, W. 2002, *ApJ*, 567, L27
- Markevitch, M., Ponman, T. J., Nulsen, P. E. J., Bautz, M. W., Burke, D. J., David, L. P., Davis, D., Donnelly, R. H., Forman, W. R., Jones, C., Kaastra, J., Kellogg, E., Kim, D.-W., Kolodziejczak, J., Mazzotta, P., Pagliaro, A., Patel, S., Van Speybroeck, L., Vikhlinin, A., Vrtilik, J., Wise, M., & Zhao, P. 2000, *ApJ*, 541, 542
- Mathiesen, B. F. 2001, *MNRAS*, 326, L1
- McNamara, B. R., Wise, M. W., Nulsen, P. E. J., David, L. P., Carilli, C. L., Sarazin, C. L., O’Dea, C. P., Houck, J., Donahue, M., Baum, S., Voit, M., O’Connell, R. W., & Koekemoer, A. 2001, *ApJ*, 562, L149

- Perlman, E., Horner, D., Jones, L. R., Scharf, C., Ebeling, H., Wegner, G., & Malkan, M. 2002, *ApJS*, in press
- Ritchie, B. W. & Thomas, P. A. 2002, *MNRAS*, 329, 675
- Roettiger, K., Burns, J. O., & Loken, C. 1996, *ApJ*, 473, 651
- Romer, A. K., Nichol, R. C., Holden, B. P., Ulmer, M. P., Pildis, R. A., Merrelli, A. J., Adami, C., Burke, D. J., Collins, C. A., Metevier, A. J., Kron, R. G., & Commons, K. 2000, *ApJS*, 126, 209
- Rosati, P., Della Ceca, R., Norman, C., & Giacconi, R. 1998, *ApJ*, 492, L21
- Sanderson, A. J. R., Ponman, T. J., Finoguenov, A., Lloyd-Davies, E. L., & Markevitch, M. 2002, *MNRAS*, submitted
- Scharf, C., Jones, L. R., Ebeling, H., Perlman, E., Malkan, M., & Wegner, G. 1997, *ApJ*, 477, 79
- Schindler, S., Castillo-Morales, A., De Filippis, E., Schwope, A., & Wambsganss, J. 2001, *aanda*, 376, L27
- Vikhlinin, A., VanSpeybroeck, L., Markevitch, M., Forman, W. R., & Grego, L. 2002, *astro-ph/0207445*
- Voit, G. M. 2000, *ApJ*, 543, 113